Title

Characterization and Applications of Laser-Compton X-ray Source

Author

Hwang, Yoonwoo

Publication Date

2018

UNIVERSITY OF CALIFORNIA,
IRVINE

Characterization and Applications of Laser-Compton X-ray Source

DISSERTATION

submitted in partial satisfaction of the requirements
for the degree of

DOCTOR OF PHILOSOPHY

in Physics

by

Yoonwoo Hwang

Dissertation Committee:
Professor Christopher Peter James Barty, Chair
Norman Rostoker Chair Professor Toshiki Tajima
Clinical Professor Dante Roa

2018

DEDICATION

To my grandfather

TABLE OF CONTENTS

Page

LIST OF FIGURES

LIST OF TABLES

ACKNOWLEDGMENTS

It would be impossible to thank all the people and organizations that have helped me though the six-year adventure, but two people in particular deserve my deepest appreciation: my UC Irvine mentor and supervisor, Toshiki Tajima, and the LLNL counterpart, Christopher Barty. It is their motivation, guidance and trust that has made my graduate school journey an exciting and meaningful one.

My two summers and 1 and a third years at LLNL have also created a long list of people I have to thank immensely; Roark Marsh and David Gibson were easily the best everyday supervisors a PhD student can ever wish. Gerry Anderson and Shawn Betts never ceased to amaze me with their knowledge and experience, in addition to being the friendliest lunchmates.

I have asked countless dumb questions that were always patiently and kindly answered by everyone at the lab, including but not limited to Felicie Albert, Scott Anderson, Scott Fisher, Fred Hartemann and Sheldon Wu. Also, many thanks to Joe and Kim who had to survey my image plates every 30 minutes when I came up from the cave with newly exposed image plates.

Back in Irvine, I shall first thank my friends – Calvin, Deano, Craig, Sahel and others – for reminding me that a graduate school can be the best place to make some of the most amazing friends. I am also grateful to Franklin Dollar and his group, saving me from being the only non-plasma person on the 4th floor on the rare occasions they were not working in their basement lab.

Of course, graduate school wouldn't have been possible without a great undergraduate experience; I cannot thank enough my undergraduate research advisor Ivan Bazarov and numerous mentors and colleagues from his group, especially Siddharth Karkare, Luca Cultrera and Rick Merluzzi. Without them, I wouldn't have known how fun accelerator physics is.

I thank immensely my family for their love and support through all the years, and I shall end the long list of acknowledgements with the most special person in my life, Agnese. Thank you for all you do for me.

CURRICULUM VITAE

Yoonwoo Hwang

EDUCATION

Doctor of Philosophy in Physics	**2018**
University of California, Irvine	*Irvine, California*
Master of Science in Physics	**2015**
University of California, Irvine	*Irvine, California*
Bachelor of Arts in Physics	**2012**
Cornell University	*Ithaca, New York*

RESEARCH EXPERIENCE

Graduate Student Researcher	**2014–2018**
University of California, Irvine	*Irvine, California*
Undergraduate Student Researcher	**2011–2012**
Cornell University	*Ithaca, New York*

TEACHING EXPERIENCE

Teaching Assistant	**2012–2014**
University of California, Irvine	*Irvine, California*

REFEREED JOURNAL PUBLICATIONS

2-D energy analyzer for low energy electrons **2015**
S. Karkare, L. Cultrera, Y. Hwang, R. Merluzzi, I. Bazarov

Review of Scientific Instruments **86**, 033301

High energy photon emission from wakefields **2016**
D. M. Farinella, C. K. Lau, X. M. Zhang, J. K. Koga, S. Taimourzadeh, Y. Hwang, K. Abazajian, N. Canac, T. Ebisuzaki, P. Taborek, T. Tajima

Physics of Plasmas **23**, 073107

Performance of a second generation X-band rf photoinjector **2018**
R. A. Marsh, G. G. Anderson, S. G. Anderson, D. J. Gibson, C. P. J. Barty, Y. Hwang

Physical Review Accelerators and Beams **21**, 073401

Electron beam characterization through K-edge filtering of laser-Compton-scattered X-rays **2018**
Y. Hwang, T. Tajima, C. P. J. Barty, D. J. Gibson, R. A. Marsh

submitted to Physical Review Accelerators and Beams

CONFERENCE PUBLICATIONS

Photocathode R&D at Cornell University **May 2012**
I. Cultrera, I. Bazarov, J. Conway, B. Dunham, Y. Hwang, Y. Li, X. Liu, T. Moore, R. Merluzzi, K. Smolenski, S. Karkare, J. Maxson, W. Schaff

International Particle Accelerator Conference 2016

Multi-bunch Operation of a Laser-Compton X-ray Source Based on Compact X-band Accelerator Technology **Mar 2016**
D. J. Gibson, G. G. Anderson, Y. Hwang, R. A. Marsh, C. P. J. Barty

Compact EUV & X-ray Sources 2016

LLNL laser-Compton X-ray characterization **May 2016**
Y. Hwang, T. Tajima, G. G. Anderson, D. J. Gibson, R. A. Marsh, C. P. J. Barty

International Particle Accelerator Conference 2016

LLNL X-band rf gun results **May 2016**
R. A. Marsh, G. G. Anderson, D. J. Gibson, Y. Hwang

International Particle Accelerator Conference 2016

LLNL laser-Compton X-ray characterization **Oct 2016**
Y. Hwang, T. Tajima, G. G. Anderson, D. J. Gibson, R. A. Marsh, C. P. J. Barty

North American Particle Accelerator Conference 2016

Electron beam diagnosis using K-edge absorption of laser-Compton photons **May 2017**
Y. Hwang, T. Tajima, D. J. Gibson, R. A. Marsh, C. P. J. Barty

International Particle Accelerator Conference 2017

Study of medical applications of compact laser-Compton X-ray source **May 2017**
Y. Hwang, T. Tajima, G. G. Anderson, D. J. Gibson, R. A. Marsh, C. P. J. Barty

International Particle Accelerator Conference 2017

Initial performance measurements of multi-GHz electron bunch trains **May 2017**
R. A. Marsh, D. J. Gibson, Y. Hwang

International Particle Accelerator Conference 2017

ABSTRACT OF THE DISSERTATION

Characterization and Applications of Laser-Compton X-ray Source

By

Yoonwoo Hwang

Doctor of Philosophy in Physics

University of California, Irvine, 2018

Professor Christopher Peter James Barty, Chair

Laser-Compton scattering (LCS) is a novel scheme of generating highly collimated synchrotron radiation-like X-ray and γ-rays with electron accelerators much smaller in size than synchrotrons. With potentials in radiography, radio-oncology and nuclear physics, laser-Compton light sources are being studied in many places. At Lawrence Livermore National Laboratory, an X-band based 30-MeV linear accelerator was built to be used as a source of electron beam for LCS studies. This thesis describes the characterization process and results of both the electron beam and the resulting X-rays of the LLNL LCS X-ray source. A new electron beam diagnostic using the K-edge absorption effect was developed using the machine and simulation tools originally used for the characterization, which is explained in detail. Next, medical applications of LCS X-ray sources are discussed, regarding K-edge subtraction method and nanoparticle Auger therapy in particular. Lastly, the dose simulations used for Auger therapy were also applied to simulating neutron capture therapy using Boron.

Chapter 1

Introduction

It would be nearly impossible to address all of the applications of X-rays since their discovery by W. Röntgen in 1895, but after more than 120 years, imaging of the human body – the very first application – and radiation therapy, which immediately followed radiology after the biological effects of X-rays became evident, are still arguably the two most widespread uses of X-rays to present day. The advancement and refinement in those two fields over the years have been nothing short of remarkable; in radiology, technological advancements in X-ray tubes and imaging system have drastically increased the diagnostic power of X-ray imaging, while development of high-contrast agents enabled real-time monitoring of the interior of the body (fluoroscopy, angiography) and rapid increase in computing power/digitization of images allowed detailed cross-section images and 3D reconstruction of the body using computed tomography. Meanwhile, advancements in accelerator technology have made possible compact X-ray sources that generate tens of MeV X-rays that are capable of rotating around the patient for stereotactic radiation therapy. The two disciplines can also be combined in image-guided radiation therapy (IGRT), where both imaging and radiation occur in the same machine.

Nevertheless, the fundamental method of X-ray generation in hospitals has not changed in the past century; the vast majority of medical X-ray sources use bremsstrahlung radiation from a beam of accelerated electrons hitting a high-Z target. Although bremsstrahlung is a very simple, compact and efficient way of generating X-rays, its essentially flat, broad spectrum is a drawback in both imaging and therapy compared to a monoenergetic source. The low energy portion of the bremsstrahlung X-rays are mostly absorbed in the first few centimeters of the skin, increasing unwanted dose, limiting the exposure time and image resolution. Furthermore, it cannot take advantage of many novel imaging methods developed using monochromatic and coherent sources, such as K-edge subtraction imaging and phase-contrast imaging. At present, synchrotron radiation (SR) from multi-GeV electron synchrotron facilities are the only source of bright, collimated and tunable monochromatic hard- X-rays; although there are a few SR facilities with active research in medical imaging and therapy, unfortunately these synchrotrons are too large and expensive to be widely available. Hence, a compact light source that can produce synchrotron-quality X-rays can have a huge impact in radiology and radiotherapy.

One of the major efforts in novel X-ray source schemes is laser-Compton scattering (LCS), also known as inverse Compton/Thomson scattering. In LCS, X-rays are generated by Compton scattering of laser light by an electron beam. The major advantage of an LCS X-ray source is that it can generate synchrotron undulator-like X-rays with a much lower electron beam energy for a given X-ray energy compared to synchrotrons, greatly reducing the footprint of the electron accelerator. In undulator radiation in synchrotrons, the electron beam passes through an alternating magnetic field created by a series of magnets with a period λ_u on the order of centimeters. From the rest frame of the electron beam, this period is shortened by a factor of γ, the relativistic Lorentz factor. As the electron oscillates under the changing magnetic field, it emits radiation in the frequency of its oscillation, therefore the radiated photons have wavelength $\lambda_e = \lambda_u/\gamma$ in the electron frame. When this radiation is observed in the lab frame, its wavelength is Doppler shifted by a factor of $\gamma(1 - \beta \cos\theta)$, where β is the speed of the electron divided by the speed of light and θ is the polar angle of the observation point with the electron's motion in the positive z direction. Therefore, the wavelength of the radiation in the lab frame is

$$\lambda = \lambda_e \gamma (1 - \beta \cos\theta) = \lambda_u (1 - \beta \cos\theta) \approx \frac{\lambda_u}{2\gamma^2}(1 + \gamma^2\theta^2) \tag{1.1}$$

in the relativistic, small observation angle limit. Therefore, the wavelength of forward radiated light is the period of the undulator reduced by a factor of $2\gamma^2$; with a 10-mm period undulator, a 6-GeV beam is necessary to make 30-keV X-rays without higher harmonics. The radiation is also collimated in the forward direction due to relativistic beaming effect; a $1/\gamma$ angle cone contains half of the total radiated flux. in LCS, the radiation mechanism is very similar except that instead of the electrons oscillating in the magnetic field of the undulators, they are oscillating due to the electric field of the laser photon. If the laser is antiparallel to the electron beam, in the electron's rest frame the laser wavelength λ_L is Doppler shifted by a factor of $\gamma(1 - \beta)$. The resulting radiation follows the same treatment as the undulator case if Compton shift is ignored, so when observed in the lab frame, the on-axis radiation wavelength is

$$\lambda = \lambda_L \gamma^2 (1 - \beta)(1 - \beta \cos\theta) \approx \frac{\lambda_L}{4\gamma^2}(1 + \gamma^2\theta^2) \tag{1.2}$$

in the same limit as above; the only difference with undulator equation being an additional factor of 2 and that the undulator period is replaced by the laser wavelength. Because laser wavelength is typically on the order of µm, there is more than a thousandfold reduction in initial radiation wavelength, which means a much lower energy electron can create the same radiated photon wavelength. With a 500-nm laser, one only needs a 30-MeV electron beam to generate 30-keV X-rays; electron linear accelerators producing 30-MeV beam are compact enough to fit in a small room and already widely used in hospitals for radiotherapy. Thus, LCS X-ray sources have the potential to make available SR quality X-rays in hospitals for vast improvements in radiology and radiotherapy, as well as other applications that can take advantage of monochromatic, tunable hard X-rays that were previously impractical due to lack of compact sources. Furthermore, the potential to create very high energy monochromatic photons in the MeV range and up creates unique possibilities for probing nuclear physics[6, 64].

1.1 Historical development of LCS sources

The scattering of electromagnetic waves by electrons was first was first explained by J. J. Thomson, and later refined by A. H. Compton who explained the increase in wavelength of scattered X-rays as a result of inelastic scattering of photons with electrons[18]. Observations of Compton scattering of laser by a beam of electrons are first reported in 1963 immediately following the invention of the laser itself in 1960[23], but due to extremely low cross section of Compton scattering and resulting low flux, the concept of using LCS as a light source had to wait until technological innovations in accelerators and lasers such as chirped-pulse amplification enabled viable X-ray output for applications, and in 1992 Sprangle et al. proposed the Laser Synchrotron Source with theoretical performance estimates and requirements for a number of applications[60]. Since then, a number of laboratories around the world have been studying LCS; some have built a high-power laser specifically for scattering with an existing accelerator, others are building new accelerator facilities dedicated for an LCS light source, and still others are also exploring LCS using electron beams produced by laser plasma wakefield, using a single high-intensity laser for both accelerating the electron beam and scattering off of the electron beam[65].

1.2 LCS X-ray Sources at LLNL

At Lawrence Livermore National Laboratory (LLNL), building 194, the 100-MeV electron linac had been used for LCS studies since the early 2000s. The first generation LCS source at LLNL, named PLEIADES for Picosecond Laser-Electron Interaction for the Dynamic Evaluation of Structures, collided a 60-MeV linac beam with an 800 nm chirped-pulse amplified laser beam to generate 70-keV X-rays with several picosecond duration[13]. Few years later, the energy of the electron beam was increased to 120 MeV and frequency-doubled (532 nm) or -tripled (355 nm) Nd:YAG interaction laser system was installed to generate up to 675-keV X-rays as a demonstration of application in nuclear resonance fluorescence detection[26]. A much more compact X-band based linear accelerator aimed at producing 30-MeV electron beam colliding head-on with a 532-nm laser to produce 30-keV hard X-rays was built in 2014. This accelerator uses the gun and one accelerating section of an originally 6-section, 250-MeV design that would have produced MeV γ-rays for NRF detection studies[3, 43].

1.3 Layout of thesis

The main topics of the thesis are 1) the characterization/optimization of the LLNL X-band accelerator and LCS X-ray system, presented in chapters 3 and 4; 2) a new electron beam diagnostic method developed using the LCS X-rays in chapter 5 and 3) prospects and simulations performed with regards to medical applications of LCS X-rays in chapter 6. In addition, Boron neutron capture therapy (BNCT) dose simulations were carried out and are described in chapter 7, using similar setups as the Gadolinium X-ray dose simulations. Theoretical background and modeling of LCS X-rays are shown in chapter 2. Finally, conclusion of the work and future outlook of LCS X-rays are summarized in chapter 8.

Chapter 2

Theoretical background and modeling

2.1 Compton scattering

Compton scattering describes the scattering of a photon by an electron. The energy of the scattered photon is easily derived by considering the scattering as a two-body collision. The equation for the conservation of energy, assuming the initial electron is at rest, reads

$$E_\gamma + m_e c^2 = E_{\gamma'} + \sqrt{p_{e'}^2 c^2 + m_e^2 c^4}, \tag{2.1}$$

where $E_\gamma, E_{\gamma'}$ denotes the initial and final photon energies, $m_e = 9.1 \times 10^{-31}$ kg is the electron rest mass, $c = 3.0 \times 10^8$ m/s is the speed of light in vacuum and $p_{e'}$ is the momentum of the electron after the collision.

Meanwhile, the equation for the conservation of momentum reads

$$\boldsymbol{p}_\gamma = \boldsymbol{p}_{\gamma'} + \boldsymbol{p}_{e'}, \tag{2.2}$$

where $\boldsymbol{p}_\gamma, \boldsymbol{p}_{\gamma'}$ denote the initial and final momenta of the photon. Squaring the above equation and solving for $p_{e'}^2$ gives

$$p_{e'}^2 = (\boldsymbol{p}_\gamma - \boldsymbol{p}_{\gamma'}) \cdot (\boldsymbol{p}_\gamma - \boldsymbol{p}_{\gamma'}) = p_\gamma^2 + p_{\gamma'}^2 - 2p_\gamma p_{\gamma'} \cos\theta, \tag{2.3}$$

where θ is the angle between the initial and final photon directions. Since $E_\gamma = p_\gamma c$, the above equation can be multiplied by c^2 to give

$$p_{e'}^2 c^2 = E_\gamma^2 + E_{\gamma'}^2 - 2E_\gamma E_{\gamma'} \cos\theta. \tag{2.4}$$

Plugging this equation into energy conservation equation and squaring both sides yields

$$E_\gamma E_{\gamma'} - (E_\gamma - E_{\gamma'}) m_e c^2 = E_\gamma E_{\gamma'} \cos\theta, \tag{2.5}$$

and solving for $E_{\gamma'}$ results in the expression for the scattered photon energy as a function of initial photon energy and scattering angle:

$$E_{\gamma'} = \frac{1}{\frac{1}{E_\gamma} + \frac{1-\cos\theta}{m_e c^2}}, \tag{2.6}$$

yielding the angle-correlated Compton shift of X-ray wavelength, with more energy loss in the backscattered direction. In the limit where the energy of the photon in the electron's rest frame is negligible compared to the electron's rest mass, there is little momentum transfer between the particles and therefore the energy of the photon can be treated as unchanging; this is known as Thomson scattering. The scattered photon energy as a function of incident photon energy and angle is shown in Fig. 2.1.

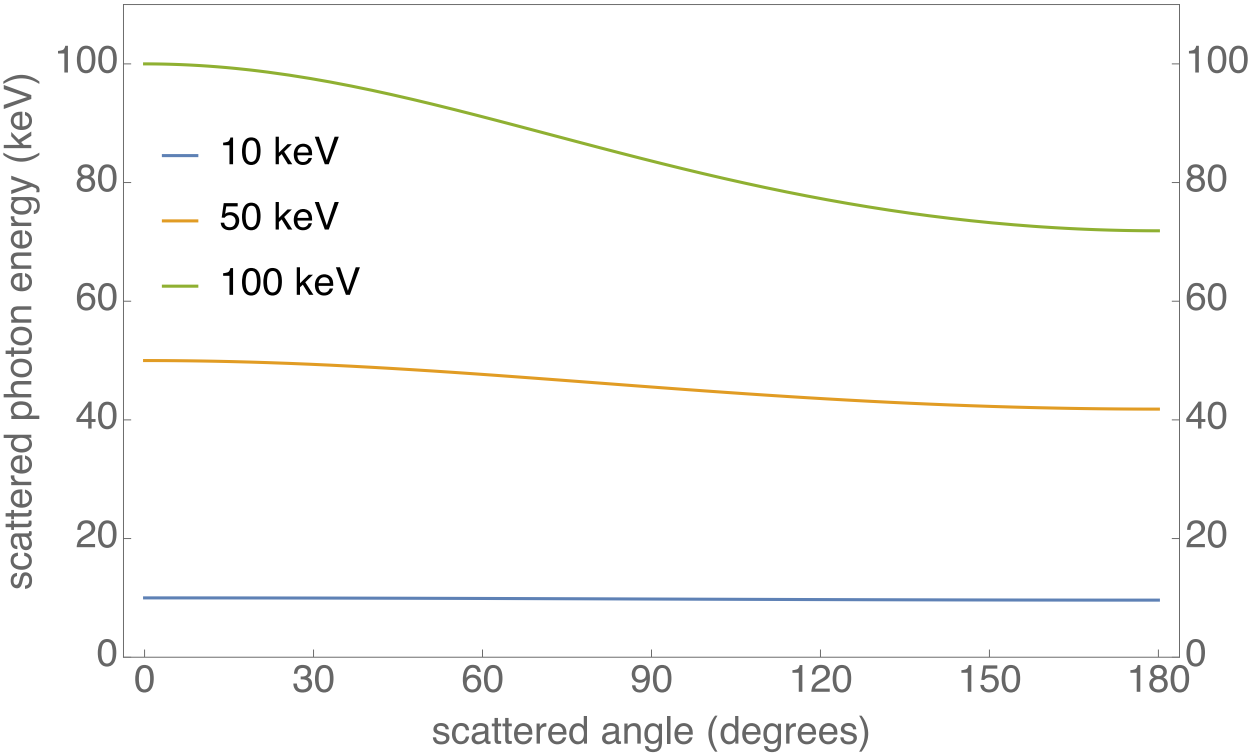

Figure 2.1: Energy-angle relationship for Compton scattered photons in the electron rest frame. Backscattered photons have greater loss in energy for higher incident energies.

As mentioned in the previous section, in LCS the energy of the incident photon in the electron's rest frame is Doppler shifted. In the case of a 180° collision, there is an energy upshift of $\frac{1}{\gamma(1-\beta)} \approx 2\gamma$. It should be noted that while the frequency upshift of photons from Compton scattering by a relativistic electron is commonly referred to as inverse Compton scattering (ICS) in astrophysics and light source communities because the scattered photons gain energy rather than lose energy, the upshift is entirely due to the Doppler effect and not the Compton effect; photons still lose energy in the electron's rest frame and the frequency upshift as seen in the lab frame is still valid in the Thomson regime. In fact, electron and photon energies in most light source applications are well below the regimes where Compton shift needs to be taken into account. For common laser frequencies in the IR-UV range, where photon energy is on the order of 1 eV, Compton shift causes less than a percent difference from that expected from Thomson scattering, which is identical to the incident energy, unless the electron beam is higher than about 500 MeV, at which point the resulting LCS photon energy will be on the order of 10 MeV. This relationship is illustrated in Fig. 2.2. Therefore, for consideration of medical X-rays in the 10 keV to 1 MeV range with relaxed bandwidth requirements, Compton effect is minimal.

2.2 Modeling of electron beam and LCS

The electron beam was modeled using PARMELA particle tracking code with which the accelerator was designed. The 6-dimensional phase space coordinates of each PARMELA macroparticles at the interaction region are used in producing the Compton-scattered X-ray spectrum and image. The laser is modeled as a perfect plane wave traveling in the z direction with its intensity modulated by a Gaussian beam envelope function. For a given observation point, the X-ray energy is found by energy and momentum conservation, while the intensity is calculated from the Klein-Nishina Compton cross section for linearly polarized photons. To account for attenuation and scintillator response, X-ray attenuation data for materials

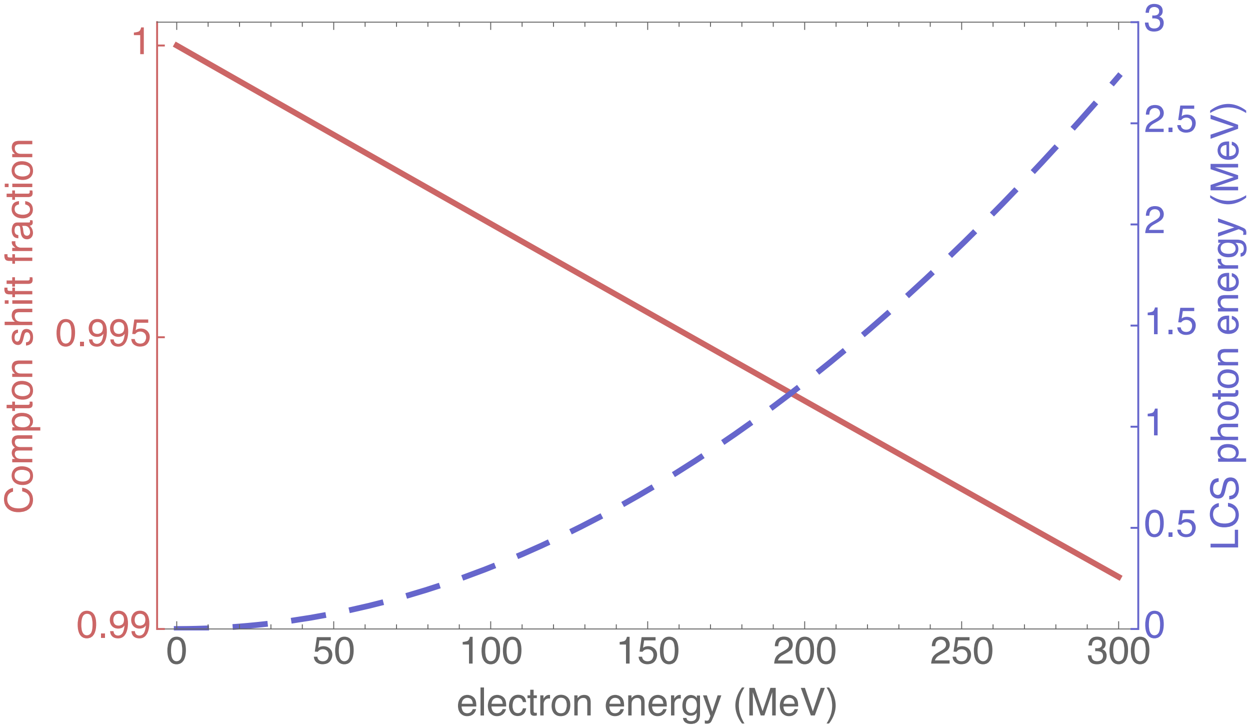

Figure 2.2: Red: ratio of scattered to incident photon energies in the rest frame of the electron for a 2 eV photon (lab frame), showing the dependence as a function of electron energy. Blue: LCS photon energy in the lab frame for a 2 eV laser photon.

encountered by the X-rays were obtained from NIST XCOM database, and for each path from the position of the electron where the X-ray photon is born to the detector pixel, the distance each X-ray photon travels within specified material was calculated and used to determine the amount of attenuation/absorption it would experience.

Chapter 3

LLNL X-band electron linac characterization

The X-band linear accelerator at LLNL produces 30-MeV, 100-pC electron beam at 10-Hz repetition rate. It consists of an 11.424-GHz rf photogun and an accelerating section powered by 50-MW klystron and a solid state modulator.

The electron beam from the X-band linac were thoroughly characterized and compared with the PARMELA model. The electron beam's spot size at the interaction point, its energy spectrum and emittance were measured and was found to be in good agreement with design parameters.

3.1 Electron beam spot size measurement

3.1.1 Introduction

The electron beams spot size and position jitter at the interaction point has been measured by processing with Mathematica the optical transition radiation (OTR) images captured with a CCD camera. Analysis of 1,000 single shot images taken on April 7 2016 yielded the average RMS width of 14.4 µm x 11.0 µm and RMS jitter of 5.11 µm x 2.77 µm.

3.1.2 Data and image processing

The data are 1,000 single shot OTR images of the electron beam on the interaction cube, taken on April 7 2016 from 11:37 to 11:40. Camera exposure was 0.1 s. There were no blanks.

The images were cropped to a 101×69 pixel region where the beam spot was present. Each image was then applied a median filter (3×3 block) and binarized with a threshold just above the noise floor (0.1%) to create a mask identifying the location of the beam. This mask was applied to the raw image after the pixel values were subtracted by the average noise value (.06%). Using the median filter when creating the mask helps masking the above-threshold noise pixel around the edge of the beam and prevents below-threshold beam pixel from being masked.

From the masked image, horizontal and vertical integrated lineouts were made, which were used to find the centroid (average position) and RMS width. The average beam size is found by averaging the RMS widths, and the RMS jitter is found by taking the standard deviation of the centroids.

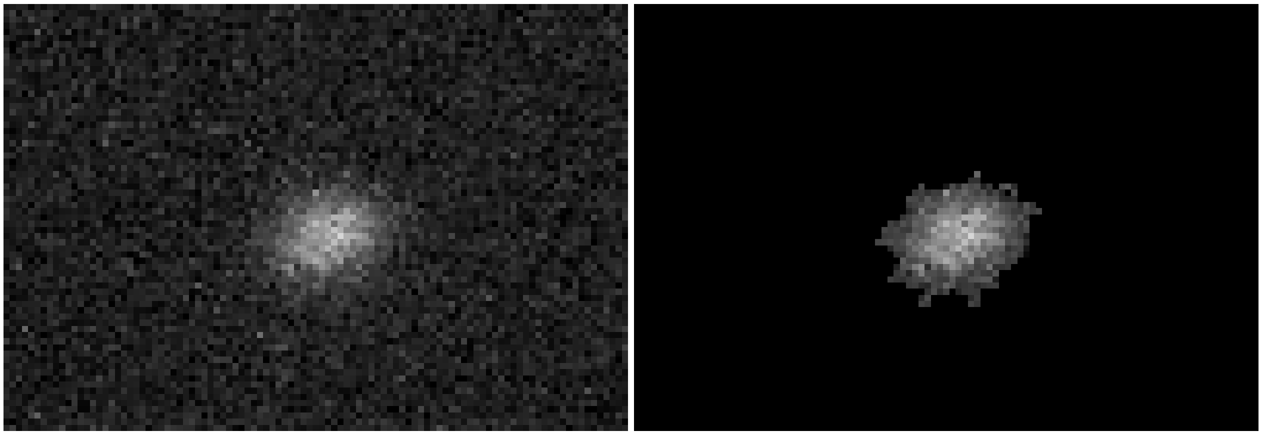

(a) (b)

Figure 3.1: Left: raw image of a single shot beam. Right: masked image.

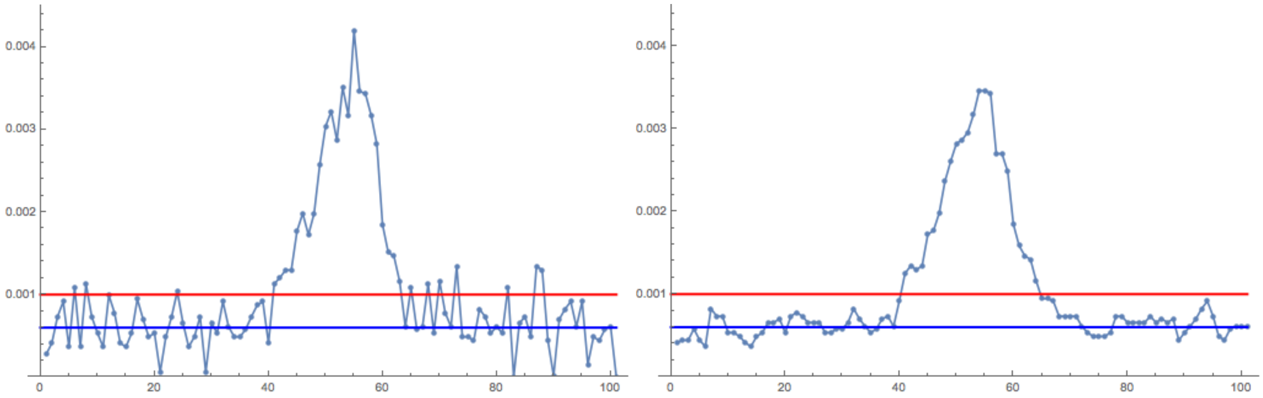

(a) (b)

Figure 3.2: Left: A raw lineout. Right: A median filtered lineout used for creating the mask. Red and blue lines indicate mask threshold and average noise value, respectively. x-axis values in pixels.

The average RMS beam width was 14.4 µm in the horizontal and 11.0 µm in the vertical; RMS jitter was 5.11 µm in the horizontal and 2.77 µm in the vertical.

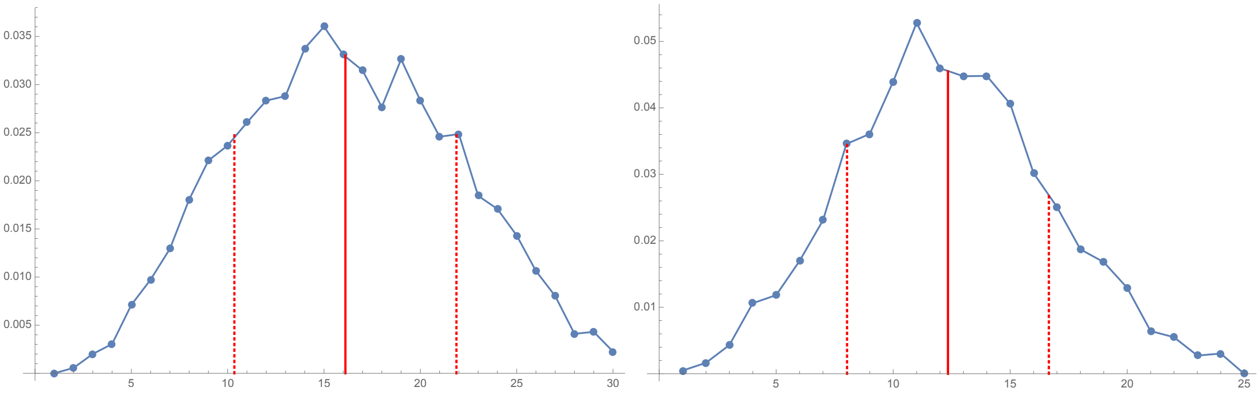

(a)

(b)

Figure 3.3: x (left) and y (right) integrated lineouts. Solid line marks the centroid position and dotted lines indicate the RMS width. x-axis values in pixels.

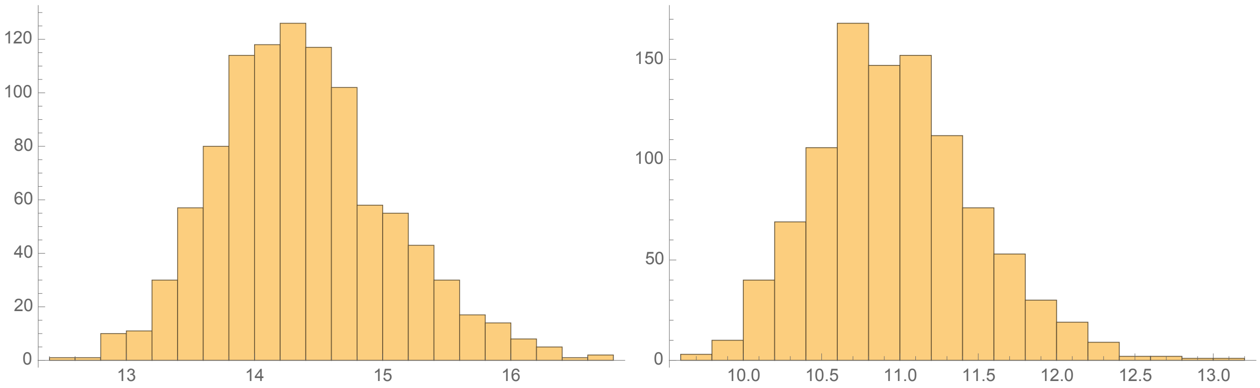

(a)

(b)

Figure 3.4: x (left) and y (right) histogram of RMS widths of 1,000 shot data. x-axis values in µm.

3.2 Spectrometer calibration and electron beam energy spread measurement

To measure the electron beams energy parameters using the spectrometer, the calibration of energy-to-position on the Yttrium Aluminum garnet (YAG) screen is necessary. Calibration was done by measuring the change in position as a function of magnetic field strength and using the relationship between the beam energy and the magnetic field.

The electron beam, after colliding with the laser photons at the interaction point, is deflected

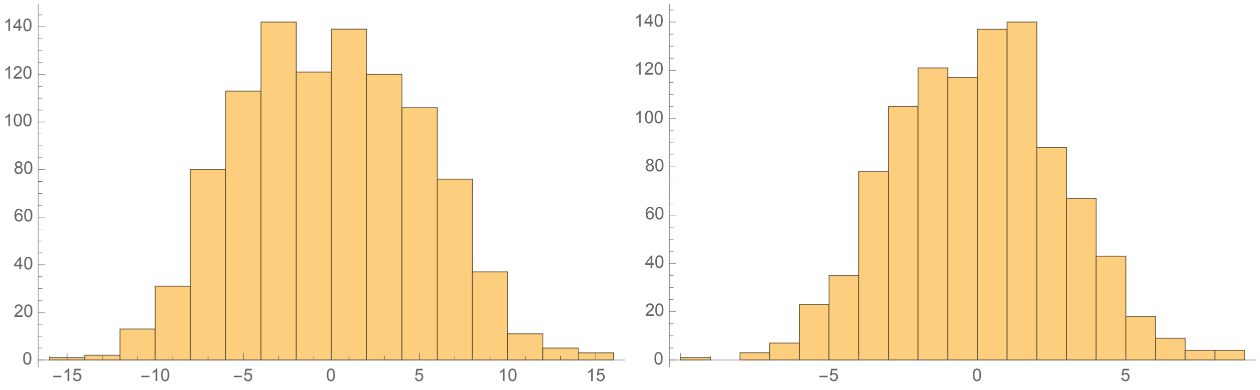

(a)

(b)

Figure 3.5: x (left) and y (right) histogram of centroids of 1,000 shot data. x-axis values in µm.

by a magnetic field from the spectrometer dipole into the beam dump. Since the amount of deflection is dependent on the energy we can measure the mean energy, energy spread and jitter from the position and shape of the deflected beam. In an idealized model, an electron with energy E in the z direction enters a a region of uniform magnetic field in the y direction of strength B. The region is a cylinder with radius r and axis in the y direction. The deflection θ is defined as the angle between the original electron direction and the deflected direction after exiting the magnetic field region. θ is related to B, E, r and fundamental constants by the equation $E = \frac{ecrB}{\tan\frac{\theta}{2}}$ where c is the speed of light and e is the elementary charge. Therefore, if B and r are known one can determine the energy of the electron by measuring the deflection angle.

3.2.1 Calibration setup

In our setup, although the spectrometer dipole does not create a perfectly uniform magnetic field with a defined radius, we can define an effective radius which, when applied to the spectrometer equation with B equaling the measured peak field, gives the same deflection as observed. The effective radius was calculated by Yeh by mapping out the magnetic field of the dipole and simulating the electron trajectory going through that field. The center field strength is inferred from a probe reading at the edge that is linearly correlated with the center field. However, the dipole setup has changed since the calibration was made, rendering the field reading less reliable than other measurable quantities r, θ and E. During operation, the spectrometer dipole is given the right amount of current to deflect the beam by 23.8° to the beam dump located approximately 2 m away, and the beam position is verified with a YAG screen in front of the beam dump. The size of the beam on the screen in the horizontal direction at its tightest focus indicates the energy spread of the beam, and the jitter of the centroid can be measured to infer energy jitter. In order to measure these quantities, the energy versus pixel calibration is necessary.

3.2.2 Calibration procedure

The calibration factor of interest is $\frac{1}{E}\frac{\partial E}{\partial x}|_B$, where x is the pixel position. Since the beam dump is fixed at 23.8°, the magnetic field changes linearly with the mean beam energy to keep the beam centered on the screen. Due to this constraint, for different mean energy E the deviation $\Delta\theta$ from θ_0 is not proportional to ΔE, but $\frac{\Delta E}{E}$. Therefore, it makes more sense to define the calibration factor in terms of relative energy spread %/pixel rather than MeV/pixel. It should be mentioned that the bandwidth and jitter are on the order of 10^{-3}-10^{-4} of mean energy; therefore, the derivatives can be considered constant and evaluated at the variables central values (θ_0, B_0, E_0) without losing accuracy. This leads to a key simplification that E and B are proportional:

$$\frac{\partial E}{\partial x}|_B \approx \frac{\partial E}{\partial B}|_\theta \cdot \frac{\partial B}{\partial x}|_E = \frac{ecr}{\tan\frac{\theta}{2}} \approx \frac{E_0}{B_0} \cdot \frac{\partial B}{\partial x}|_E \Rightarrow \frac{1}{E}\frac{\partial E}{\partial x}|_B = \frac{1}{B_0}\frac{\partial B}{\partial x}|_E \tag{3.1}$$

This equation is the basis of our calibration, and it is convenient because the magnetic field value does not need to be the real field value; as long as it is proportional to the real value by some factor, that factor cancels out in the end. Therefore, readings from the probe were taken directly in the calculations of B_0 and $\frac{\partial B}{\partial x}|_E$, which was measured by varying the dipole current and recording the change in the field versus the beam position. On the other hand, in order to measure the mean energy, precise measurement of B is necessary. As an interim solution until the probe is recalibrated, B was inferred from an independent measurement of beam energy. E_0 was estimated from the size of the hole of the Compton X-ray Sn foil K-edge image. Using $E_0 = 28.6$ MeV, $\theta_0 = 23.8^\circ$ and $r = 17.3\,\text{cm}$, it yielded a value about 10% less than the probe readings.

To measure $\frac{\partial B}{\partial x}|_E$, 1,000 single shot images of the beam were made at the central position of $B_0 = 1284$ G (probe reading) and also at two other magnet settings, 1276 G and 1287 G respectively. The centroids of the images were found using the same Mathematica code as described in the electron beam source size measurement section, with adjustments in initial crop size and noise floor appropriate for the beam dump camera. The centroids were -263 pixels / +132 pixels away from the reference point for the 1276 G / 1284 G, respectively. The three data points were fitted to yield $\frac{\partial B}{\partial x}|_E = 0.028$ G/pixel. Using the above equation, the calibration factor was calculated to be 0.0022%/pixel.

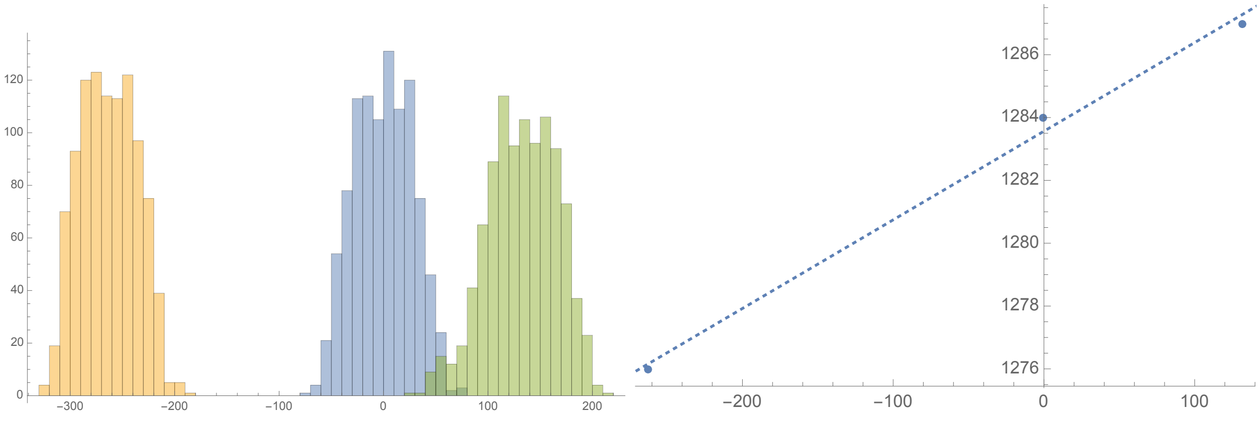

(a) (b)

Figure 3.6: Left: centroid histogram for three spectrometer settings. Right: fitted line of $\frac{\partial B}{\partial x}|_E$

3.2.3 Energy spread and jitter measurement

The spread (bandwidth) and jitter in the electron beam energy was measured assuming the horizontal position at the beam dump screen was dominated by the chromatic effect from the dipole and not the beams transverse properties. The energy spread is then the width of the spot, while the jitter is the width of the distribution of the centroid. The RMS energy spread was found to be 0.031%, and RMS jitter was 0.061%.

3.3 Emittance measurement

The emittance of the beam was measured via quadrupole scanning method. A quadrupole triplet located just after the accelerating section was used to focus the beam, which travels down a straight section of about a meter before it hits a YAG screen that images the beam. 10-20 single-shot data were collected per magnet strength, which are processed by a MATHEMATICA code that measures the horizontal and vertical beam size as well as the standard deviation for each data point.

The beam size can be determined in 3 ways: direct RMS calculation from the beam centroid, a Gaussian fit and a supergaussian fit. direct calculation is the fastest but also most prone to different background levels and noise. A Gaussian fit is more insensitive to noise, but the beam is usually not a Gaussian; therefore a supergaussian fit, which has an additional free parameter at the exponent that can adjust the pointedness or flatness of the profile, was also used. Since nonlinear fits using a 4-parameter supergaussian model can be time-consuming, a Gaussian fit was first found then its centroid, normalization and width fits were fed into the supergaussian fit's initial guess. Once the beam size information at each magnet strength were found, the data were fitted to find the Twiss parameters of the beam.

The normalized transverse emittance at 80 pC was about 0.3 mm-mrad with optimized emittance compensation solenoid settings.

Chapter 4

Characterization of X-rays

The output LCS X-rays' flux was measured using a calibrated X-ray CCD camera. Also, the source size of the X-rays were measured with the CCD camera; the resolution limit of the scintillator/CCD system limited the exact measurement of the source size.

4.1 Calibration of Andor X-ray CCD camera

Since the laser-Compton X-ray machine aims to produce state-of-the-art X-ray beams, the importance of X-ray diagnostics cannot be stressed enough. Currently, the only equipment being used for characterizing the X-ray beam is the Andor CCD camera. This is an indirect method utilizing an ICCD camera coupled to a scintillator plate via fiber optics. Since the scintillator photon output, which is proportional to CCD count, is roughly linear with input X-ray photon energy and not the number of X-ray photons, the quantity the camera measures is spatial energy distribution and not number distribution. The indirect measurement implies the photon density distribution can be extrapolated from the image only if the spatial spectral distribution is known. Accordingly, the calibration factor is CCD count per absorbed energy.

The calibration is carried out by irradiating the camera with a radiation source of known activity and radiation characteristics and comparing the theoretical absorbed energy with the CCD counts. The accuracy of this calibration is crucial, as photon flux, one of the most important qualities of X-ray machines, is calculated from it.

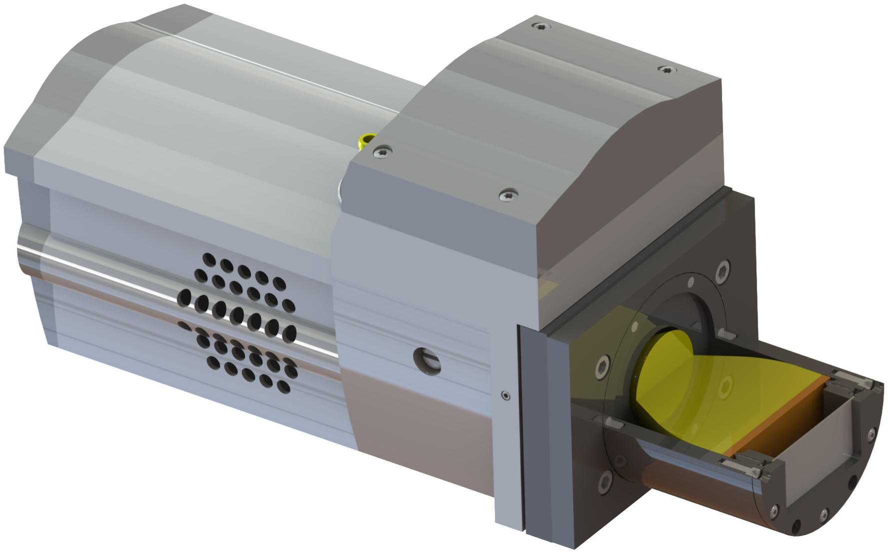

Figure 4.1: CAD image of the Andor camera with cutaway of the scintillator section

4.1.1 Setup and method

Scintillator & camera assembly

The camera has a 40-mm × 40-mm wide, 0.5-mm thick Beryllium window in front of the scintillator to block low energy noise. Two scintillators were available for use; a 175 µm thick CsI(Tl) on a fiber optic plate and a 310–µm thick $Gd_2O_2S:Tb$ phosphor screen. Theoretical spectral response curves for both setup were calculated and plotted in Fig. 4.2 using photon yield references[66, 20, 50, 63] and NIST XCOM data[9]. Publications on the photon yield of CsI(Tl) vary from 45 photons/keV to 66 photons/keV and there is slight non-proportionality[29, 46], but knowing the photon yield is unnecessary for the purpose of calibration and using a calibration source emitting X-ray energy near the energy of interest can reduce the error associated with the nonlinearity of response.

The CsI plate/Gd_2O_2S:Tb screen is pressed on to a 3:1 fiber taper, which is in turn attached to the image intensifier. The image intensifier is a photocathode coupled with a microchannel plate (MCP), which adjusts the gain by changing the applied voltage between the two ends. A phosphor screen is placed after the MCP to transform the electrons back to photons, which then travel through a fiber optic connected to the CCD. The detector is 18 mm in diagonal, 1024x1024 pixels with 16-bit resolution, and is thermoelectrically cooled.

The incoming X-ray photons will be attenuated by the Beryllium plate and the scintillator along the way, and only the photons absorbed by the scintillator (some will penetrate since the scintillator is very thin) will be detected on the CCD. The attenuation A is in the units of cm^2/g, such that when multiplied by the density ρ gives the inverse of the attenuation length λ. A beam traveling a distance x inside a material will be attenuated by a factor of $e^{-\frac{x}{\lambda}}$. For the case of the scintillator, the X-ray beam is first attenuated by the Beryllium plate then absorbed by the scintillator, so the absorbed intensity I is given by

$$I = I_0 e^{-\frac{d_{\mathrm{Be}}}{\lambda_{\mathrm{Be}}}}(1 - e^{-\frac{d_{\mathrm{scint}}}{\lambda_{\mathrm{scint}}}}), \tag{4.1}$$

where I_0 is the incoming intensity and λ_α is the attenuation length of the material α. The values for the densities used were $\rho_{\mathrm{Be}} = 1.85\ \mathrm{g/cm^3}$, $\rho_{\mathrm{CsI}} = 4.51\ \mathrm{g/cm^3}$ and $\rho_{\mathrm{Gd_2O_2S}} = 4.68\ \mathrm{g/cm^3}$. Multiplying each radiation intensity by its energy and summing all up yields the total energy deposited on the scintillator.

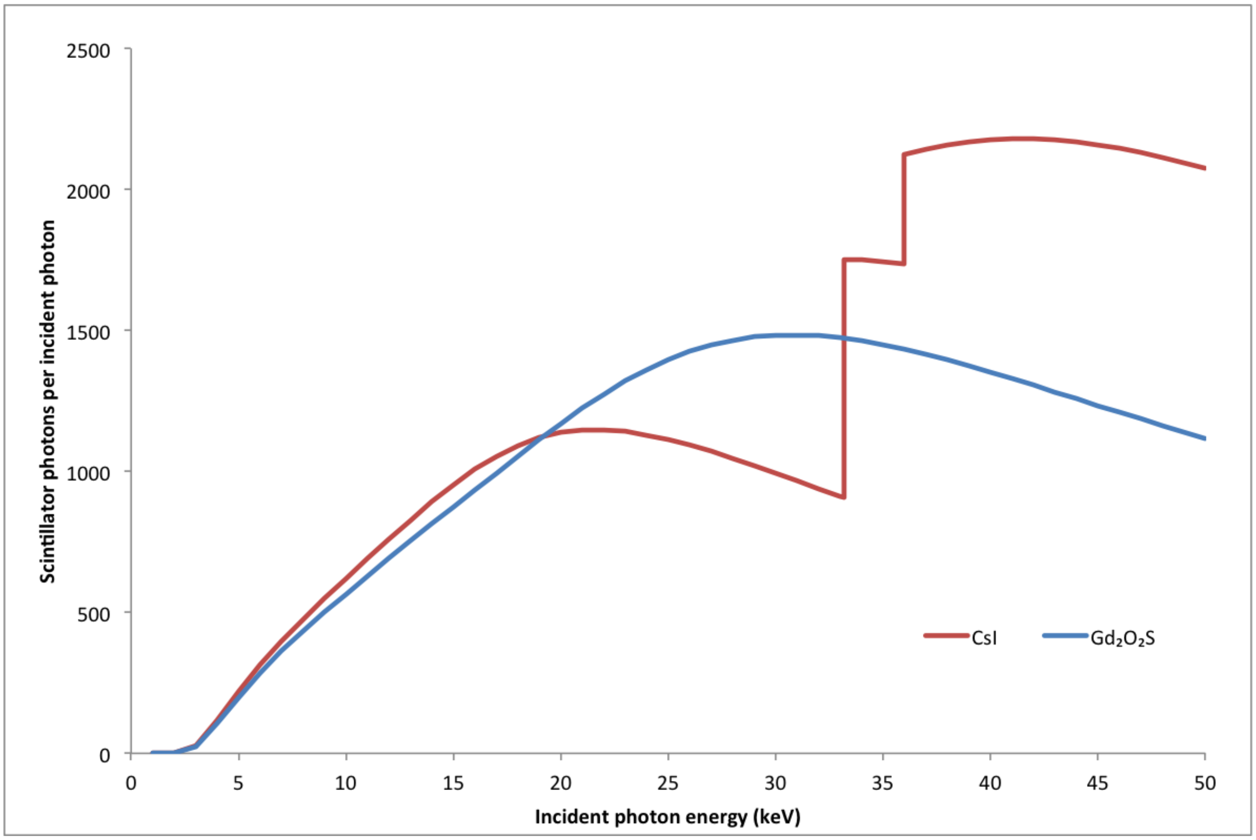

Figure 4.2: Theoretical spectral response of the beryllium-scintillator assembly, using NIST XCOM data and assuming a linear photon yield of 66 photons/keV for CsI and 60 photons/keV for Gd_2O_2S Due to the scintillator's thinness, absorption efficiency is less than 100% for higher energies and thus there are features such as decreasing photon yield for higher energies and pronounced steps at the K-edges of cesium (36.0 keV) and iodine (33.2 keV).

Calibration source & solid angle calculation

A sealed ^{129}I radioisotope source was obtained from the B194 inventory. This isotope was found to be most suitable for calibration among the available sources since its radiation is concentrated around 30 keV γ-rays, corresponding to the output photon energy of the laser-Compton source. Table 4.1 shows the emission spectrum of ^{129}I. The activity of the source was documented as 5.02 µCi.

The source is sealed inside a 1-inch diameter, 1/4-inch thick disc of plastic. The exact location

E (keV)	3.6-5.4	29.5	29.8	33.6	34.5	39.6
Photons per 100 decays	7.9	20.1	37.2	10.3	2.30	7.42

Table 4.1: X-ray and γ-ray emissions spectrum of ^{129}I[7]

and size of the source is crucial in calculating the solid angle of the detector and thus the number of incident photons. The dimensions of a similar sealed source by a different manufacturer was retrieved from the internet, but this serves nothing more than a reference and cannot be used for calculation of the solid angle.

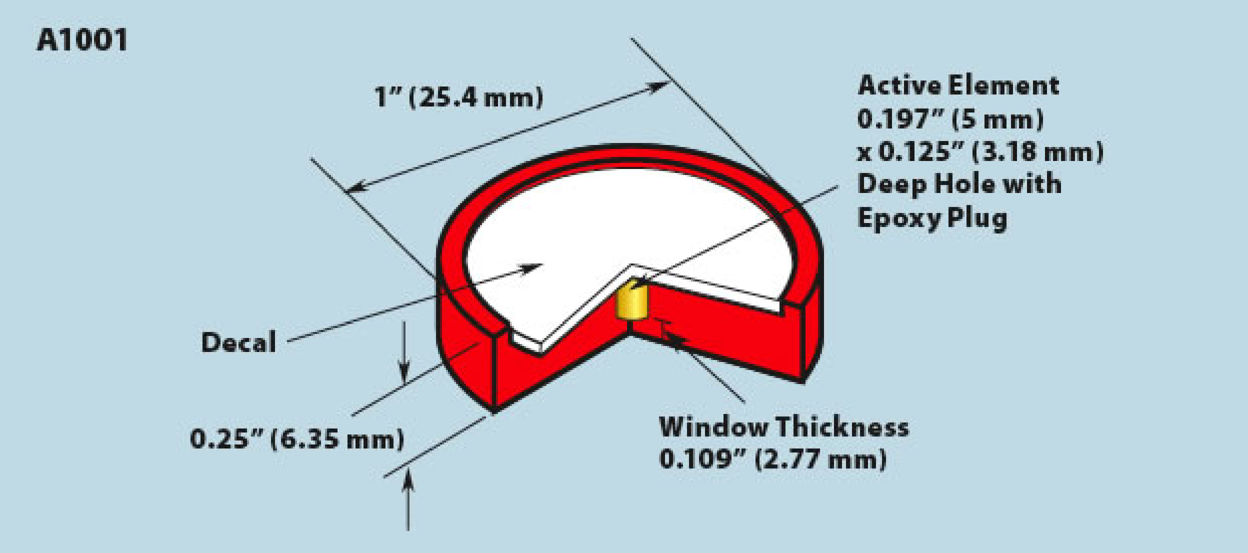

Figure 4.3: Dimensions of a disc sealed source from http://www.drct.com/dss/sources/gammasources.htm

In addition, the distance between the source and the scintillator cannot be directly measured due to the presence of the beryllium plate, so the error would have been larger than acceptable, especially since the source had to be placed as close as possible to the camera for maximum signal and thus increased the relative size of the uncertainty. Hence, rather than estimating the source radius and distance to the camera, the data was taken at several distances and a fit to several distance-solid angle curves were made with different source radii. The measurements were done at 30-s exposure, over a distance of 20 mm for Gd_2O_2S and 28 mm for CsI at 2-mm intervals using a translation stage. The distance from the scintillator to the source at the closest point will be denoted as the offset distance henceforth, and it is this offset value that would need to be found based on the fit to the theoretical model. Two runs were done for each scintillator; first placing the source closest to the camera and moving it away, then another set going back towards the camera. The theoretical solid angle model is based on a calculated table for a disc source and a disc detector[25]. To match the disc detector configuration, only the central 20-mm radius circular region of the 40-mm × 40-mm image was used for counting the CCD counts.

Background characterization

The camera has a thermoelectrically cooled CCD, but it cannot keep the temperature constant and the noise increases with time. Since the calibration signal is not very strong at far distances, correct background subtraction is very important when trying to find a fit to the model. Through background takes over extended period of time it has been verified that the noise increases roughly linearly for at least the first hour of operation, though the initial value and slope were different from run to run.

4.1.2 Results

Best fit parameter for the offset distance was found for solid angle profiles assuming different source radius from 0 to 10 mm. It was found that the offset distance did not change much as a function of the source radius; the solid angle varied by less than 3% from point source approximation to 10-mm radius. Therefore, using a nominal value of 2.5 mm, corresponding to the diagram in Fig. 4.3, was justified.

The average calibration factors for the two sets were 29.75 counts/keV for CsI and 107.4 counts/keV for Gd_2O_2S.

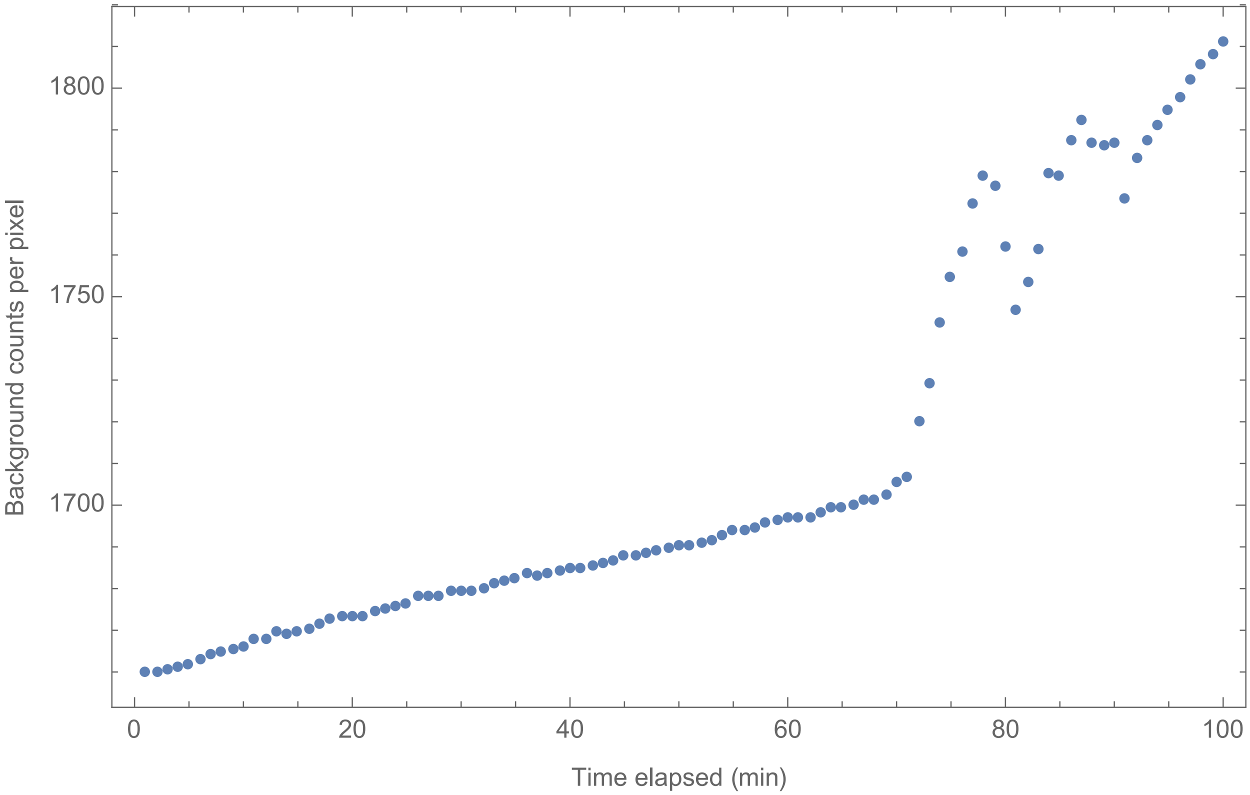

Figure 4.4: Trend of background counts over time of 30 s exposure takes.

	CsI away	CsI towards	Gd_2O_2S away	Gd_2O_2S towards
offset (mm)	19.49	21.06	19.66	24.50
counts/keV	29.48	30.01	98.15	116.6

Table 4.2: offset distance fits and calculated calibration factor for each set of data.

The offset distance changed considerably between the set moving away from the camera and the set moving towards the camera, especially for the Gd_2O_2S runs. For the set moving away, the offset value was 19.66 mm but for the set moving towards, the value was 24.50 mm. For comparison, in the CsI measurement the values were 19.49 mm for moving away and 21.06 mm for moving towards. Both measurements show a larger offset fit for the set moving towards, which were done after the set moving away. The immediate cause of this is that background-corrected counts are consistently less for the later set, making the later set flatter than the preceding set. The solid angle profile is flatter in the more distant region, so the offset fit value becomes larger. It seems that the rate of the background increase based on the

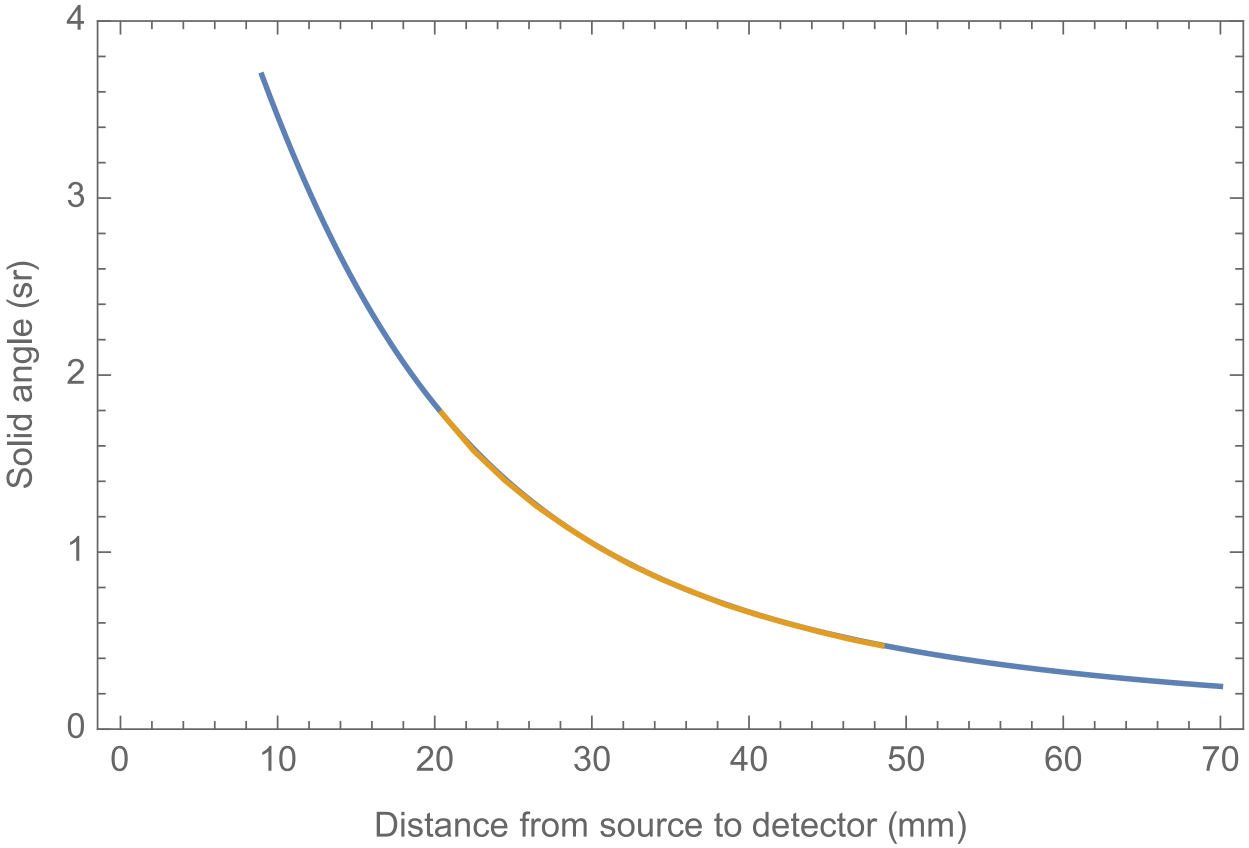

Figure 4.5: Solid angle onto a 20-mm radius disc detector subtended by a 2.5-mm radius disc source for varying distances. Blue line is data from Gardner et al.; orange line is CsI calibration data normalized and given offset of 19.5 mm to fit the theoretical curve.

background takes is higher than what the combined data suggests in order to match them. It is also possible that the slope decreases slightly as time elapses. More background takes should have been taken to accurately characterize the background behavior. The background slope can be manipulated such that the two sets are matched at the same locations, and might yield a more accurate calibration value than simple averaging of the results.

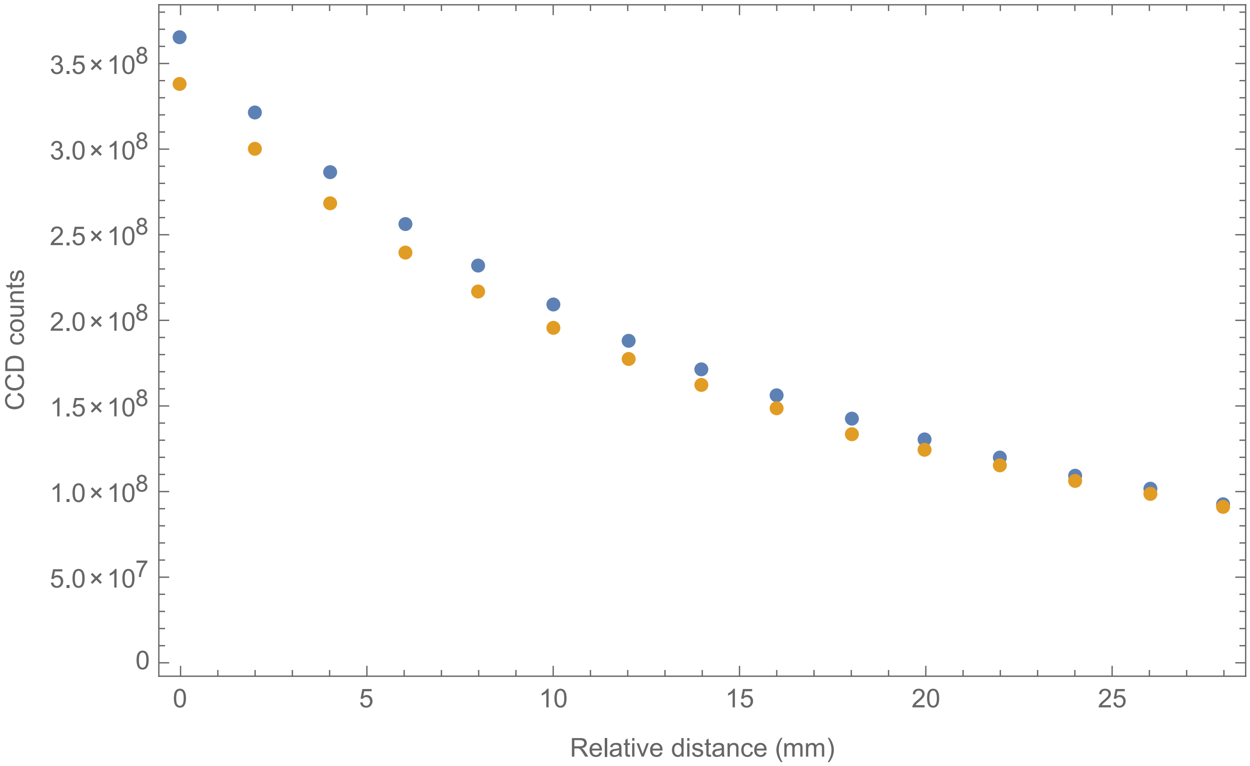

Figure 4.6: Background-corrected CCD count data for CsI calibration. Blue points were measured starting from 0 to 28, then orange points were measured moving backwards. The discrepancy between the two sets are more pronounced as time elapses, indicating incorrect background subtraction.

4.2 X-ray flux calculation and comparison with theory

4.2.1 Simulation of interaction

The X-ray simulation code calculates the spectrum and intensity of Compton-scattered X-rays within a cone of desired solid angle, centered on the laser axis. The input electrons come from PARMELA. The mean energy of the simulation was 30 MeV; it was subtracted by a constant to match experimental data using silver K-edge images. Likewise, the charge is not the value used for the PARMELA simulation but instead set to match the daily log data as it is only used as a flux scaling factor, along with interaction laser energy.

The simulation was set to calculate the X-ray spectrum within a 4 mrad diameter aperture.

The spectrum is then multiplied by transmission ratios of materials along the beam path, namely the back-thinned optic, two Berylllium windows and the absorption ratio of the scintillator (CsI or Gd_2O_2S) for the corresponding energies. The absorption data of materials were taken from NIST XCOM. Calculating the area under the curve of this absorption spectrum gives the total X-ray energy absorbed by the scintillator, which is predicted to be proportional to scintillator photon yield, which in turn is predicted to be proportional to CCD counts. The CCD counts per absorbed energy has been calibrated for the two types of scintillators using an ^{129}I radiation source, which emits photons mostly in the 30-40 keV range. Thus, possible error due to spectral nonproportionality are minimized as long as the output X-ray is in the same range. The exception to this is near the K-edges of I and Cs (33.2 keV and 36.0 keV, respectively) where absorption and light yield of the CsI scintillator may be severely disproportionate.

The simulation predicted 4900 photons per shot within the 4-mrad cone with mean energy of 25.9 keV. The total absorbed energy per shot is 48 MeV for Gd_2O_2S and 34 MeV for CsI. Using the calibration factors, these numbers correspond to 5.81 and 1.00 million counts, respectively. The actual numbers used for comparison is different for every set because the charge is taken from logged data.

4.2.2 Experimental results

The X-ray images were taken with exposure times between 1 s and 60 s. Since the system runs at 10 Hz, these images are integrations of 10-600 shots. Between August 18 2015 and September 1 2015 the data were taken with Gd_2O_2S but after September 3 15 the scintillator was replaced with CsI and the camera was moved further back, increasing the size of the 4 mrad region of interest. The images are background-subtracted, but an additional rectangular region in the image that should not contain signal was sampled and subtracted the counts from the rectangular region from that of the 4-mrad region, adjusted for the area difference. This rectangular background was 5% of signal for the noisiest 1-s images and less than 1% for most others.

The best flux was achieved on August 20 2015. Six 10-s images of mostly increasing flux were taken between 15:25 and 16:10. The charge was logged at 16:15. Two 1-s images were taken at 16:35, after which silver foil was put in to see the K-edge effect. Flux analysis on images with silver foil was not attempted since the center region contains low signal to noise ratio and very sensitive to e-beam energy/distribution which are difficult to measure. The CCD counts from the 8 images were compared with calculation from theory using 55-pC bunch charge, the average of logged charge. The 10-s images showed flux of up to 69% of theoretical value, while the 1 s images were higher: up to 113% of theory were measured.

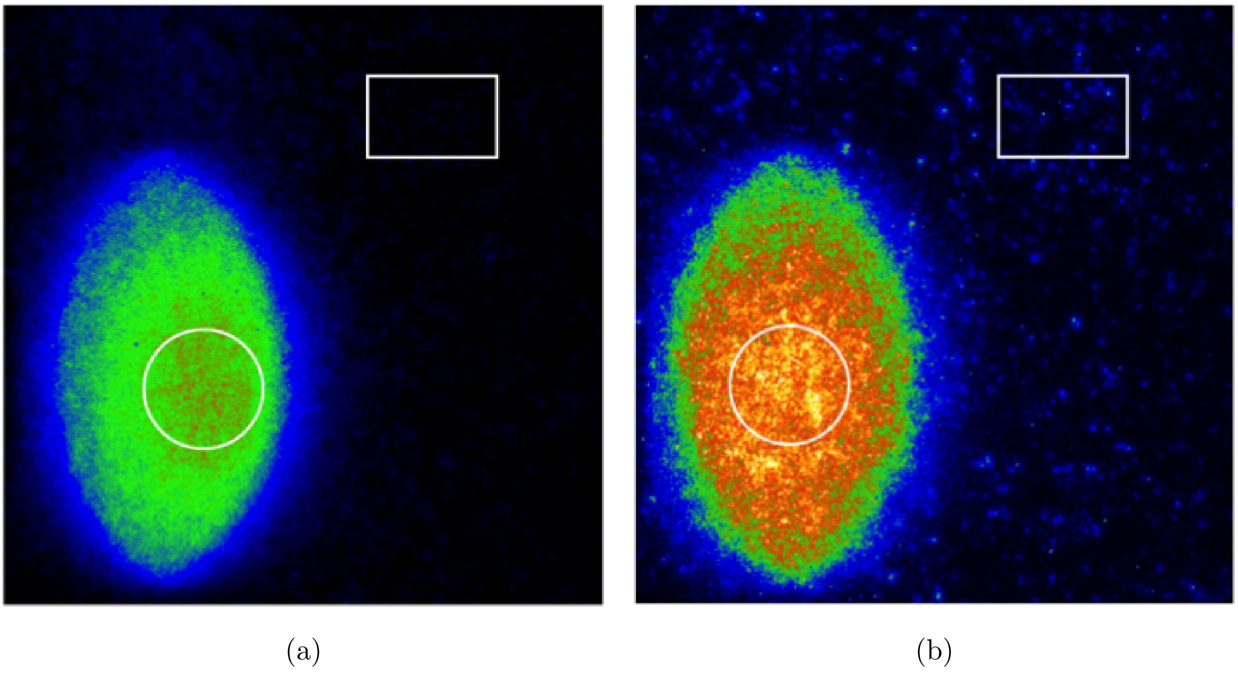
(a) (b)

Figure 4.7: Left: A sample 10-s integration image of the X-rays, with a 4-mrad cone region for flux measurement denoted with a white circle and a background subtraction region in white rectangle. Right: A sample 1-s integration image.

4.3 Source size characterization

4.3.1 Background

Small X-ray source size is a characteristic of Compton light sources that is of particular importance in several imaging applications such as phase contrast imaging[12], but accurate source size measurement has yet to be achieved due to the limited imaging capability of the current setup.

The spatial resolution of a radiograph depends strongly on both the source size and the imaging system's resolving power. The source size of our X-ray beam is similar to the size of the electron spot size at the interaction point, since the electron spot size is smaller than the laser spot size. The RMS source focal spot size σ_s can be defined from the geometric unsharpness formula $\sigma_s = \sigma_p a/b$, where σ_p is the RMS penumbra size, a is the source to object distance and b is the object to detector distance. Modeling of radiographs using the image simulation code described in [33] shows excellent agreement of the above-defined source size and the electron beam spot size.

Single shot OTR images of the electron beam spot at the interaction point show an RMS size of 14 µm in horizontal and 11 µm in vertical, with jitter around 5 µm by 3 µm[41]. The integrated image of 1,000 overlapped shots (Figure 4.8) yields 16.7 µm by 12.8 µm and is very close to Gaussian in profile (Figure 4.9).

Therefore, in order to measure the penumbra and the X-ray source size directly, a very high resolution imaging device is necessary; otherwise the blur from the imaging system will dominate the resolution of the result, rendering source size determination impossible. The large field-of-view Andor X-ray CCD camera that was used to characterize the beam's flux and bandwidth is not capable of resolving small details necessary for the source size measurement, due to scintillator thickness, 3:1 demagnification fiber optic taper and multiple

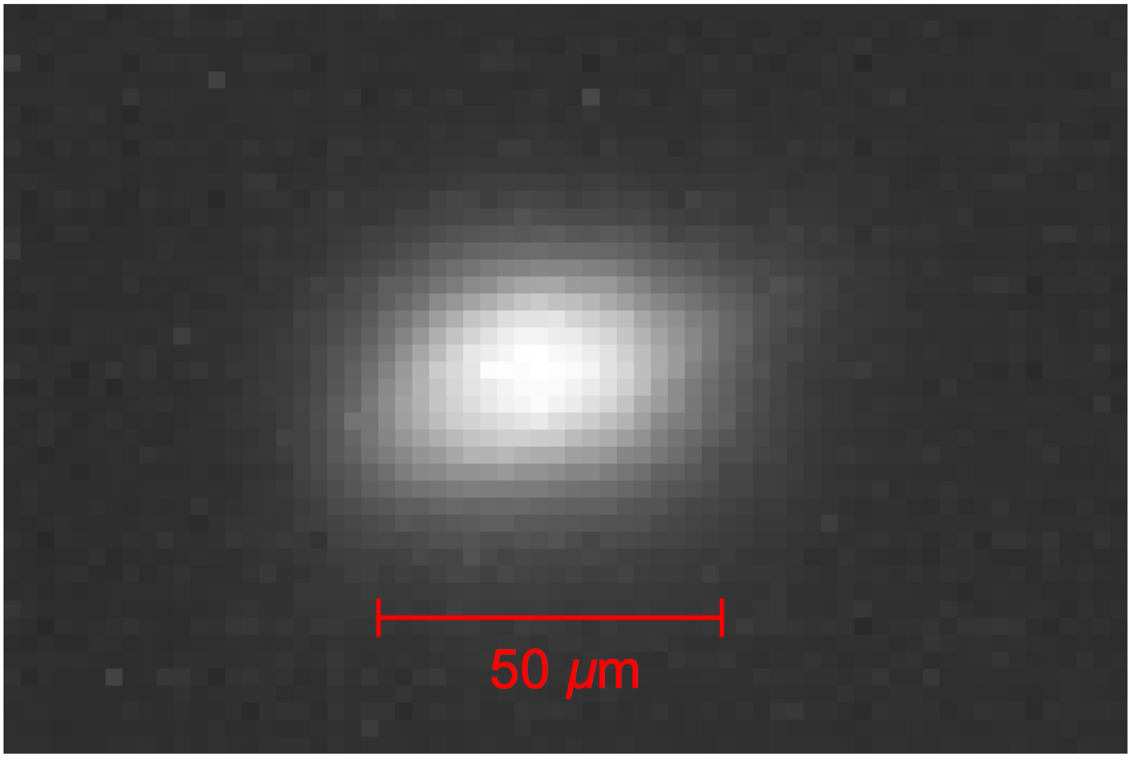

Figure 4.8: 1,000 shot OTR image of the electron beam at the interaction point.

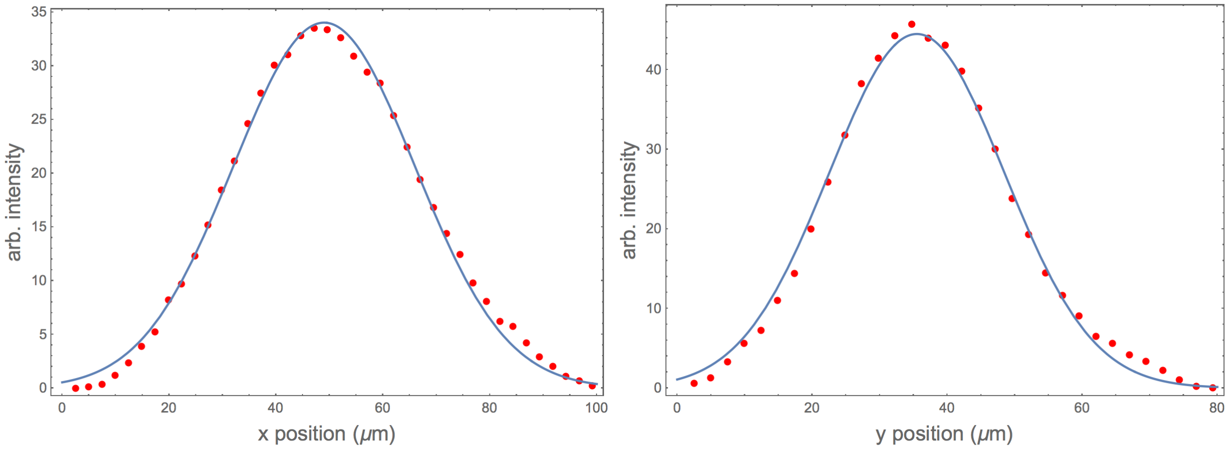

Figure 4.9: Integrated lineout profiles in red and their Gaussian fits in blue in the horizontal (left) and vertical (right) directions of Figure 4.8.

fiber optic relays, in addition to dimmed and non-uniform sensitivity of the CCD owing to extensive radiation damage from previous Compton scattered γ-ray experiments[26]. The spatial resolution of the camera measured with a sharp edge varied between 350 μm and 700 μm FWHM depending on the scintillation material used. We have purchased a new

CCD camera with a thin scintillator and lens relay system allowing 11 µm spatial resolution from Crytur, which is expected to be delivered shortly. Meanwhile, we have characterized the beam using another Andor camera identical to our current camera in a slightly different setup, with a 150 µm CsI scintillator and without the 3:1 taper. The pixel size is 13 µm with field of view of 13 mm by 13 mm.

4.3.2 Measurement of spatial resolution of the imaging system

To measure the resolution of the camera, a wedge-type line pair gauge etched from 30 µm thick Lead was placed directly in front of the scintillator. This eliminates the penumbra from the source, and the sharp edges of the resolution test pattern are blurred solely due to the imaging system. Figure 4.10 shows the resulting image captured by summing 100, 30-s exposure images, for a total exposure time of 50 minutes. Sample lineout profiles at 6.9 lp/mm and 10.4 lp/mm is shown in figure 4.11.

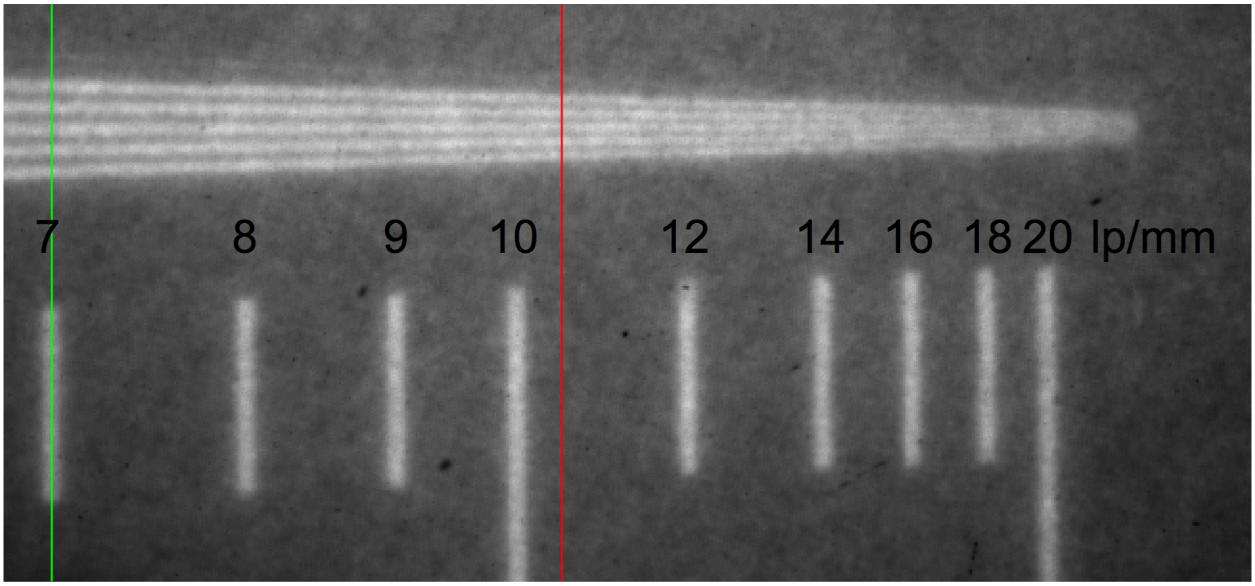

Figure 4.10: 50 minute integration image of the resolution test pattern at unity magnification.

A fit of the lineout was made by convolving a square wave function of appropriate frequency

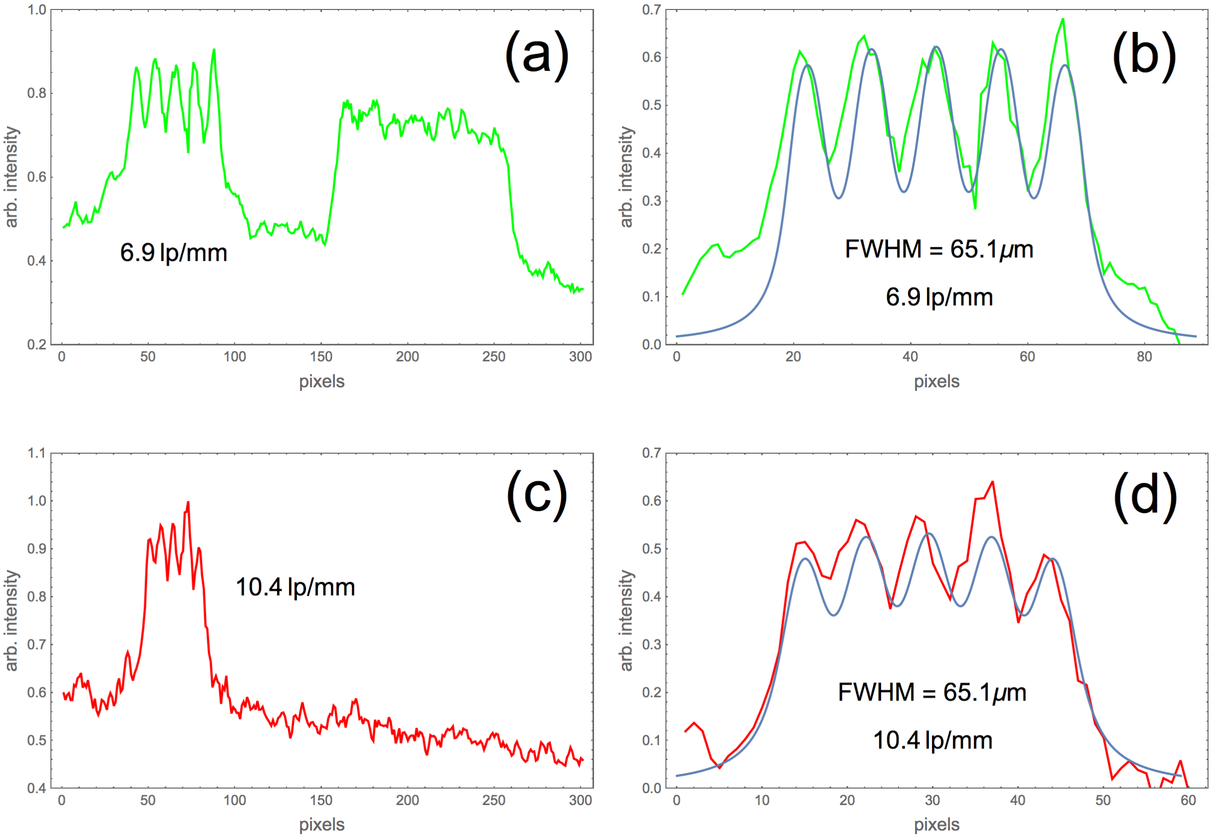

Figure 4.11: Lineout profiles of Figure 4.10 (a,c) and their Cauchy distribution convolution fit in blue (b,d).

representing the line pairs with a Cauchy distribution of varying FWHM. Image blurring in the scintillator is a result of X-ray photons creating electron-hole pairs which then travel along the crystal as they migrate to impurity centers where energy is given off as visible light[48], and therefore the point spread function is highly pointed with long tails, justifying the use of Cauchy distribution as the fitting function. A blur of 65-µm FWHM Cauchy distribution was found to fit the data well across most frequencies; this is regarded as the upper bound since the resolution could be smaller if signal to noise was better.

4.3.3 Measurement of source size

For the source size measurement, the line pair gauge was placed as close as possible to the X-ray source (laser-Compton interaction point) to create maximum magnification and penumbra. The image was magnified 1.7x, and the corresponding imaging simulation showed that the blurs in line pair images at this distance can be well approximated by a Gaussian blur with $\sigma = 0.7\sigma_e$, where σ_e is the RMS width of the electron beam. Hence, the fit was made by convolving square wave functions with a Gaussian distribution kernel, then further convolving it with a 65-µm Cauchy distribution kernel. The resulting image and the fits of two sample lineouts are shown in Figures 4.12 and 4.13 respectively. The image was acquired by summing 75, 1-minute integration images, for a total exposure time of 75 minutes.

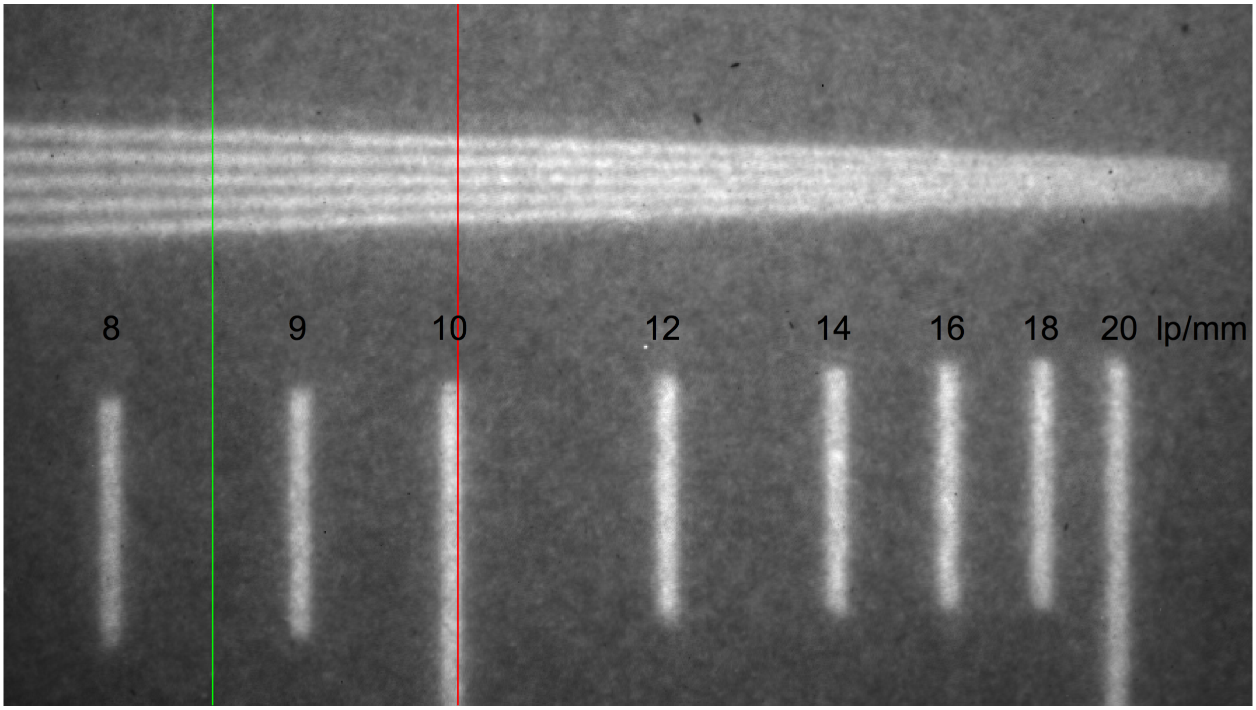

Figure 4.12: 75 minute integration image of the resolution test pattern at 1.7x magnification.

The upper bound for Gaussian σ in the fit was 30 µm, corresponding to a maximum source size (and electron beam size) of 42-µm RMS, or 100-µm FWHM. This upper bound value is much higher than the measured electron beam size due to limitations in the imaging system;

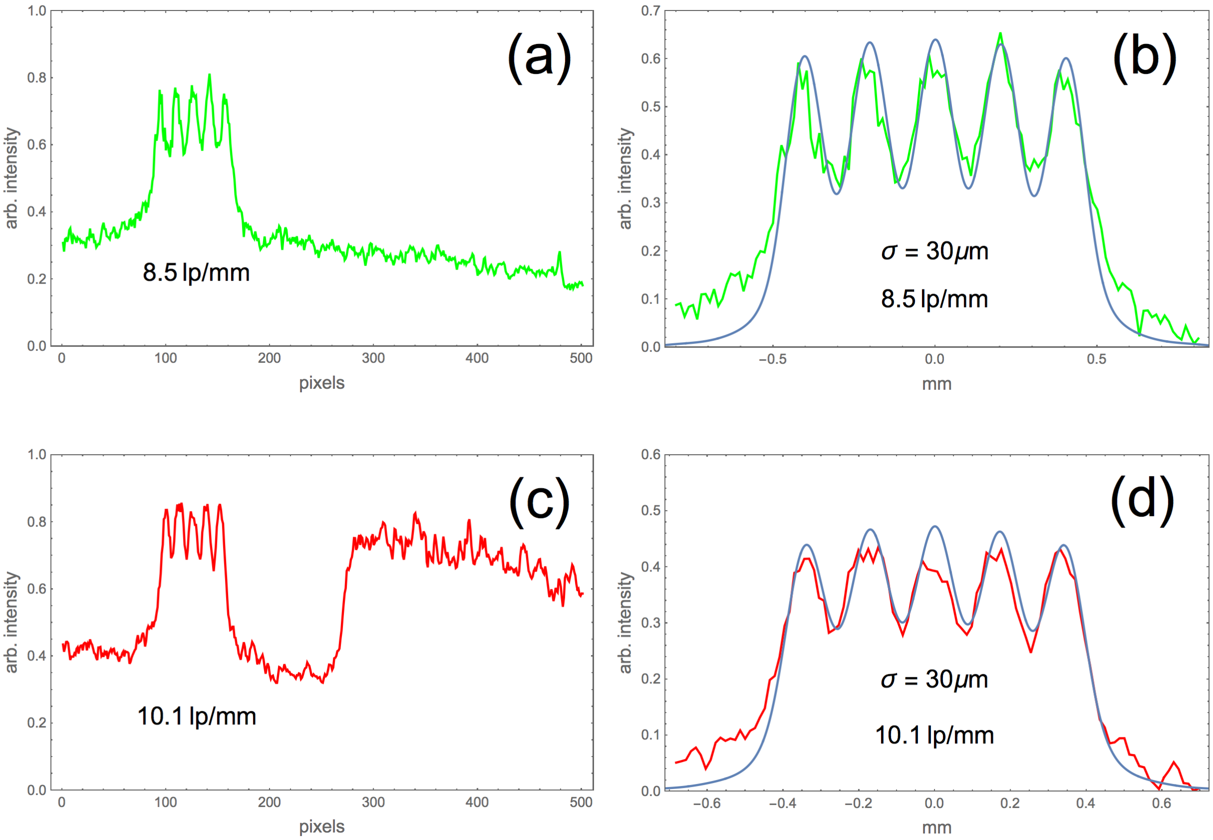

Figure 4.13: Lineout profiles of Figure 4.12 (a,c) and their Gaussian+Cauchy distribution convolution fit in blue (b,d).

the scintillator blur is of comparable size and the signal-to-noise ratio is low as evidenced by the image.

4.3.4 Conclusion

X-rays produced from the Laser-Compton X-ray source at LLNL have been thoroughly characterized; the flux and bandwidth match well with simulation results. Advancements in direct measurement of the source size has been made through a new camera setup and modeling analysis despite the limited resolution of the imaging system.

Chapter 5

Electron Beam Characterization Through K-edge Filtering of Laser Compton-Scattered X-rays

5.1 Introduction

Soon after the invention of the laser, Fiocco and Thompson[23] observed Thomson scattering of laser by an electron beam. Since then, in addition to being studied extensively as compact, high-energy X-ray and γ-ray sources[60, 24, 47], laser-Thomson/Compton scattering (LCS) X-rays have been used as diagnostics for plasmas and beams. When scattered by a relativistic electron beam, the laser photons are Doppler shifted to very high energies, often in the X-ray and γ-ray regimes and highly collimated in the direction of the electron beam. Due to the strong dependence of LCS X-rays on electron beam quality, the photons have been used to characterize almost all electron beam parameters of interest, including transverse and longitudinal beam size[59, 5, 2, 39, 27], divergence[39, 17, 27, 35], energy spectrum[49, 37, 17, 61, 27, 35, 13] and polarization[4, 28]. Majority of the electron beam energy and divergence measurement involves measuring the spectrum of the Compton X-rays using conventional X- and γ-ray spectroscopy – scintillator/semiconductor single-photon counting or Bragg diffraction – and comparing the spectrum with a simulated spectrum created by an electron beam with expected parameters. Nevertheless, even if precise measurement of the spectrum is unavailable or unfeasible, one may still be able to determine the LCS spectrum using filter attenuation methods, such as Ross filters[15, 53] or attenuation through variable thickness materials[32]. An even simpler method is to use a filter material whose K-edge is slightly below the on-axis LCS X-ray energy, so that the center of the beam, where the energy is higher, would be strongly attenuated while the outer regions are not. This method has been used to verify the energy of LCS X-rays[13, 69]. It is therefore logical to investigate the possibility of extending this technique to measuring the electron beam parameters and compare the precision against other methods, especially spectrum-resolved LCS methods. In this section, I present the mechanisms of our K-edge filtering diagnostic technique and the simulation tool, and the experimental setup and results conducted using Lawrence Livermore National Laboratory (LLNL)'s 30-MeV X-band linac to verify the technique.

5.2 Laser-Compton scattering beam diagnostics

5.2.1 Compton scattering from a relativistic electron

The physics of Compton scattering of laser by a relativistic electron or a beam of electrons have been extensively studied. Two most important differences from scattering from a stationary electron are that the scattered photon is twice Doppler-shifted to very high energies, and that the Lorentz transform from the electron frame to the lab frame causes the scattering cross section to be highly collimated in the direction of the electron's momentum, producing a narrow beam of high energy photons. The energy E_γ of a Compton-scattered photon from a collision with a relativistic electron is

$$E_\gamma = \frac{\gamma - \sqrt{\gamma^2 - 1}\cos\phi}{\gamma - \sqrt{\gamma^2 - 1}\cos\theta + k_0 \lambdabar_c (1 - \cos\theta\cos\phi + \cos\psi\sin\theta\sin\phi)} E_L, \tag{5.1}$$

where γ is the electron's Lorentz factor, ϕ is the angle between the incident electron and the laser photon, θ is the angle between the incident electron and scattered photon, ψ is the angle between the incident and scattered photons, k_0 is the wave number of the incident photon, $\lambdabar_c$ is the reduced Compton wavelength of the electron and E_L is the incident photon energy[1]. In the head-on collision ($\phi = \pi$) with an ultra-relativistic electron, this equation can be approximated in the small observation angles ($\theta \ll 1$) as

$$E_\gamma \approx \frac{4\gamma^2}{1 + \gamma^2\theta^2 + 4\gamma k_0 \lambdabar_c} E_L. \tag{5.2}$$

In this form, contributions from different components are manifest. The $4\gamma^2$ factor is due to the double Doppler upshift, while the second and third terms in the denominator represent energy reductions from off-axis scatter and Compton recoil, respectively. The reduction in photon energy due to Compton recoil is significant only when the incident photon energy in the electron frame is comparable to the electron rest mass. As mentioned earlier, scattered light is strongly focused in the forward direction as a result of relativistic beaming. Figure 5.1 shows the Compton-scattered spectrum and energy-angle correlation for a 532-nm photon colliding head-on with a 25.5-MeV electron ($\gamma = 50$). It is clearly seen that the right half of the spectrum is contained within a $1/\gamma$ =20-mrad cone.

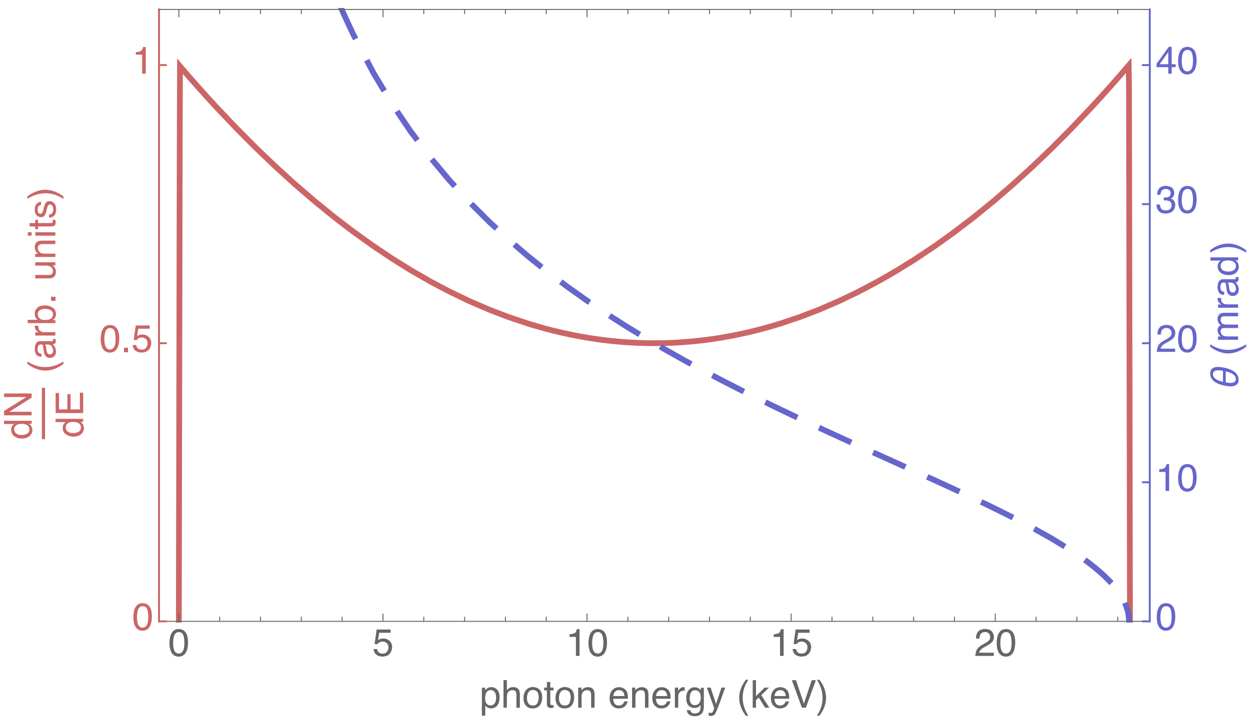

Figure 5.1: Energy spectrum (solid) and scattering angle (dashed) of photons Compton-scattered from a 25.5 MeV electron ($\gamma = 50$).

5.2.2 Compton scattering from an electron beam

When a beam of electrons interacts with an intense laser, the energy-angle correlation is blurred due to multiple factors; particles traveling in different directions (divergence), particles having different energies (energy spread), multiple scattering and nonlinear effects due to high laser intensity all contribute to broadening of the local spectrum at a given observation angle[31, 14]. Among them, the electron beam's divergence σ_θ and energy spread σ_E tend to dominate the broadening effect in typical setups where nonlinear effects are negligible and the laser bandwidth is smaller than the electron energy spread. Clearly, such reduction in coherence is detrimental in LCS light source applications; in order to control the broadening effects, much effort has been put into understanding how beam parameters affect the scattered spectrum. This knowledge can be applied backwards to deduce the electron beam parameters from the LCS spectrum.

Beam divergence and energy spread affect the local spectrum in different ways[35, 56], and is demonstrated in the simulations of X-ray spectrum in Fig. 5.2. Two different electron beams were simulated; a divergence-dominated beam with $\sigma_\theta = 1\,\text{mrad}$, $\sigma_E = 0.06\,\%$ and an energy spread-dominated beam with $\sigma_\theta = 0.2\,\text{mrad}$, $\sigma_E = 0.5\,\%$. The mean energy is $29.1\,\text{MeV}$ for both beams. The figures on the upper half are from the divergence-dominated beam, while the ones on the lower half are from the energy spread-dominated beam. The angular-spectral distributions are shown on the left, local spectra at various detector angles θ_d are shown in the middle and integrated spectra within various cone angles are shown on the right. The white dotted lines in the angular spectrum plots indicate the energy-angle correlation for a reference electron having $E = 29.1\,\text{MeV}$ and no divergence. θ_d is measured from the electron beam axis, which is antiparallel to the incident laser beam.

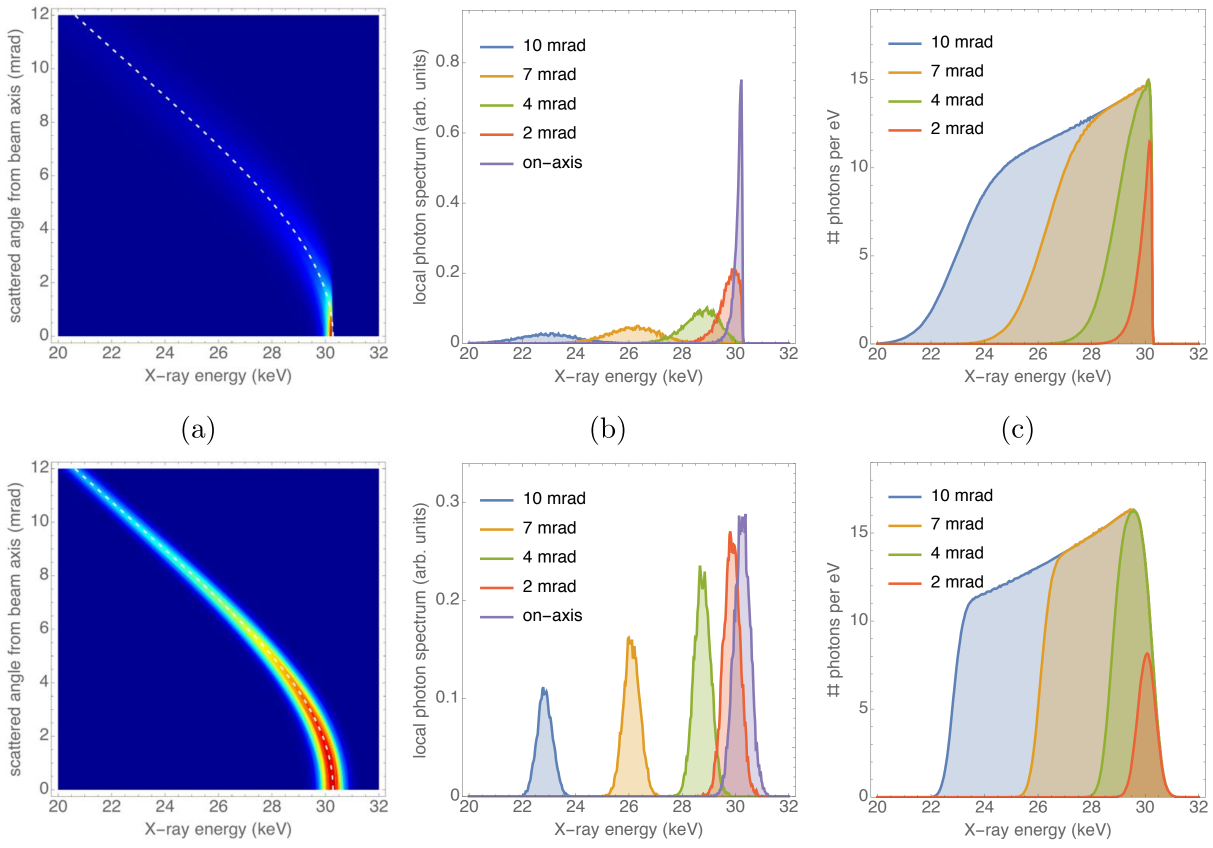

(a) (b) (c)

(d) (e) (f)

Figure 5.2: Angle-resolved spectrum (left), local spectra (center), integrated spectra (right) for divergence-dominated beam (top) and energy spread-dominated beam (bottom).

The shape of the local spectrum from the divergence-dominated beam, shown in Fig. 5.2b, is sharp with a hard edge at the upper end for $\theta_d < 1\,\mathrm{mrad}$, but becomes progressively wider further off axis. The dramatic change in bandwidth is because the energy-angle correlation is relatively flat for small angles until it takes a steep descent at around $\theta_d \approx \frac{1}{10\gamma} = 1.75\,\mathrm{mrad}$. Thus, as long as the divergence of the beam is less than $1/10\gamma$ as in this example, the on-axis spectrum's narrow bandwidth is preserved, while the off-axis spectrum bandwidth is greatly affected by σ_θ. One of the most distinguishing features of a divergence-dominated beam is the steep cutoff on the high-energy side of the integrated spectrum, since the scattered photon energy is insensitive to small variations in laser-electron collision ϕ. In other words, the X-ray spectra from different electrons appear identical despite the difference in collision angles, only differing in direction.

On the other hand, the local spectrum from the energy spread-dominated beam is mostly a reproduction of the spectrum of the electron beam, and the shape changes very little with negligible bandwidth increase for increasing observation angles. As a result, the on-axis bandwidth is higher than that of the divergence-dominated beam, but the off-axis bandwidth is narrower, leading to a steeper cutoff at the lower end of the integrated spectrum and a gradual slope matching that of the electron energy spread at the higher end.

5.2.3 Measuring the LCS spectrum

It is clear that measuring the LCS spectrum will reveal information about the electron beam's spectrum and divergence[36], and its precision can be greatly enhanced if spectra from multiple observation points are available. Once the X-ray spectra are obtained, one can reconstruct the electron beam by simulating the Compton scattering of that beam with the laser and matching the resulting X-ray spectrum to the experimental data. Numerous experiments have measured the LCS spectra at multiple observation angles[1, 16], and some have resulted in quantitative determination of beam parameters[17, 35, 27]. Most experiments obtained the local angular spectra using single photon counting methods, either by scanning a single detector along the observation angle[17, 1], or via spectroscopic imaging, where each pixel of a CCD[35] or a photodiode array[27] measures the energy of incoming photons. Bragg diffraction from crystals[51, 16, 57] have also been used to measure the angle-resolved X-ray spectra, which has several advantages over single photon counting method since limitation on flux due to pile-up is eliminated, and the angular spectrum is obtained in a single image. Lastly, Ross filter[55] is an established X-ray spectroscopic technique utilizing the K-edge absorption effect, and multiple laboratories have proposed and used the method for LCS spectroscopy[15, 53]. However, the bin sizes of a Ross filter spectrometer, which are equal to differences in K shell edge energy of adjacent elements, are typically about 1 keV and thus too crude for the purpose of electron beam reconstruction.

5.3 K-edge filter method

Brown *et al.*[13] demonstrated that filtering the LCS X-ray with a material whose K-edge lies slightly below the maximum energy can produce a dark spot or a 'hole' in the center of the X-ray image because of the energy-angle correlation of LCS X-rays, and also noticed that the sharpness of this center spot gradient depends strongly on beam divergence and energy. In that work, the maximum X-ray energy varied from 73 keV to 78 keV and a Ta foil with a K-edge at 67 keV was used. Later, similar K-edge filter techniques were used to confirm the energy of the LCS source at BNL-ATF[69, 58].

Building on aforementioned works, we extended the K-edge hole method to measure the beam energy spread and divergence. The variation in intensity profile of a filtered image was found to be very sensitive to the three electron beam parameters; we determined these parameters by adjusting the simulation beam parameters to match the data. In this way, one need not measure the X-ray spectrum directly; the full angular intensity distribution compensates for the lack of spectral information.

5.3.1 beam effects on K-edge hole

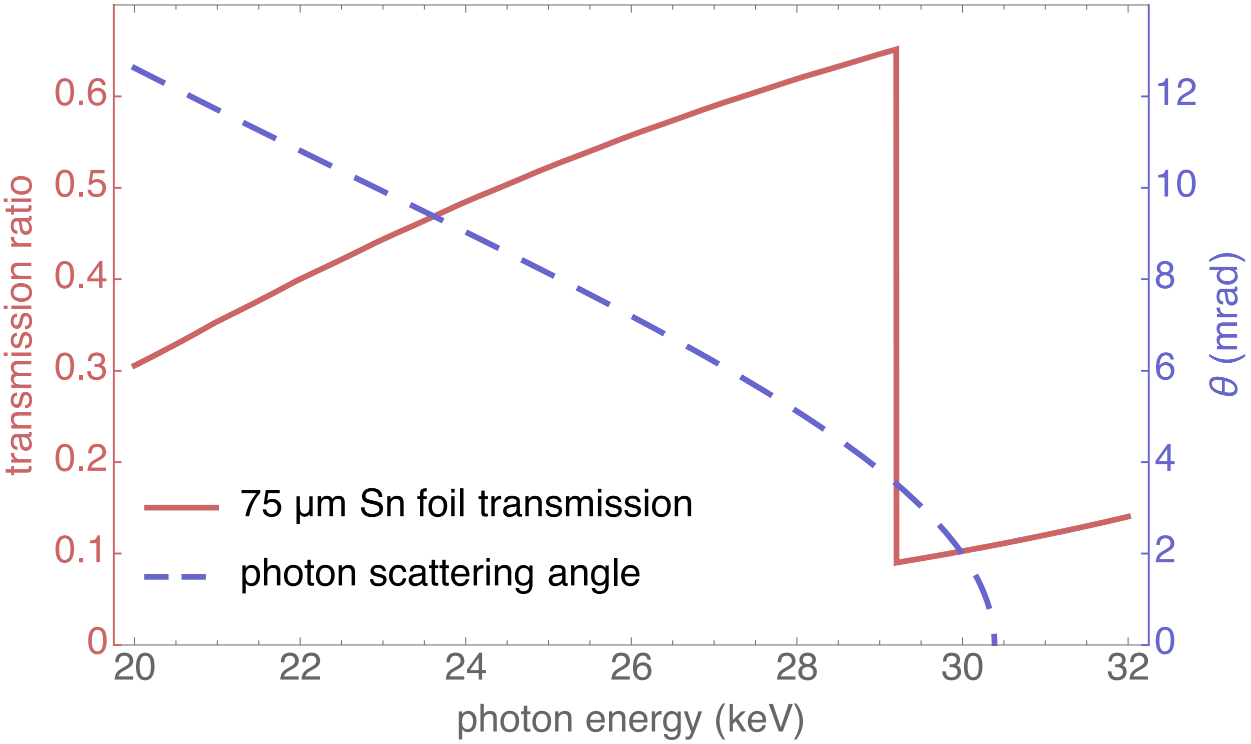

Figure 5.3: X-ray transmission ratio (solid) through 75-µm thick Sn foil showing the K-edge at 29.2 keV and X-ray scattering angle-energy relationship (dashed, cf. Eq. 5.2) from a head-on collision of 532-nm photon and 29.1-MeV electron beam which crosses the Sn K-edge energy at 3.4 mrad.

A simulated image of a Compton X-ray flux distribution from a single electron is shown in Figure 5.4a. The vertical profile lineout through the center is plotted to the right. The observation angle is defined from the laser beam axis, and the electron direction is antiparallel to the laser direction. The electron's energy is 29.1 MeV, corresponding to $1/\gamma = 17.5$ mrad. The incident laser is linearly polarized in the horizontal direction which is responsible for the vertically oblong shape. With an incident laser photon wavelength of 532 nm (2.33 eV) and a head-on collision geometry, the on-axis backscattered photon energy is 30.3 keV. Figure 5.4b shows the same X-rays filtered by a 75-µm thick Sn foil. The foil's attenuation spectrum and the X-ray energy-angle function are plotted in Fig. 5.3. A significant attenuation is visible within the central region bounded by a circle with a radius of observation angle $\theta = 3.4\,\mathrm{mrad}$, corresponding to the angle at which the scattered X-ray energy is equal to the Sn K shell energy E_K= 29.2 keV, and can be found be rearranging Eq. 5.2 for θ with E_K replacing E_γ:

$$\theta = \sqrt{\frac{4E_L}{E_K} - \frac{1}{\gamma^2} - \frac{4k_0\lambdabar_c}{\gamma}}. \tag{5.3}$$

The hole size is thus an indicator of electron energy given fixed laser wavelength; higher electron energy results in a larger hole. Obviously, if the maximum (on-axis) scattered energy is less than the K edge, there will be no sharp hole.

Since the sharp edge of the hole is due to the energy-angle relationship, when there is spectral broadening the edge is softened, as some photons in the observation point will be above the K-edge while others are not. In the case of spectral broadening due to multiple electrons as discussed in section 5.2.2, the softening effect can be explained as a result of a superposition of single electron hole intensity distributions that vary in hole size and position. When the laser is scattered by a beam of electrons with nonzero energy spread, each electron contribution has a slightly different hole radius according to Eq. 5.3. Figure 5.4c shows the hole image when the electron beam has a 0.5% Gaussian energy spread. On the other hand, when the electron beam has nonzero divergence, each electron creates a hole centered on its own direction of travel rather than the laser-defined observation axis. Figure 5.4d shows the 3.4-mrad hole blurred due to 1-mrad Gaussian beam divergence.

In the K-edge hole beam diagnostic, the beam parameters are found by first obtaining a filtered LCS X-ray image and fitting the image using simulations with ansatz beam parameters. In this demonstration, vertical profile through the center is used for checking the fit. In figure

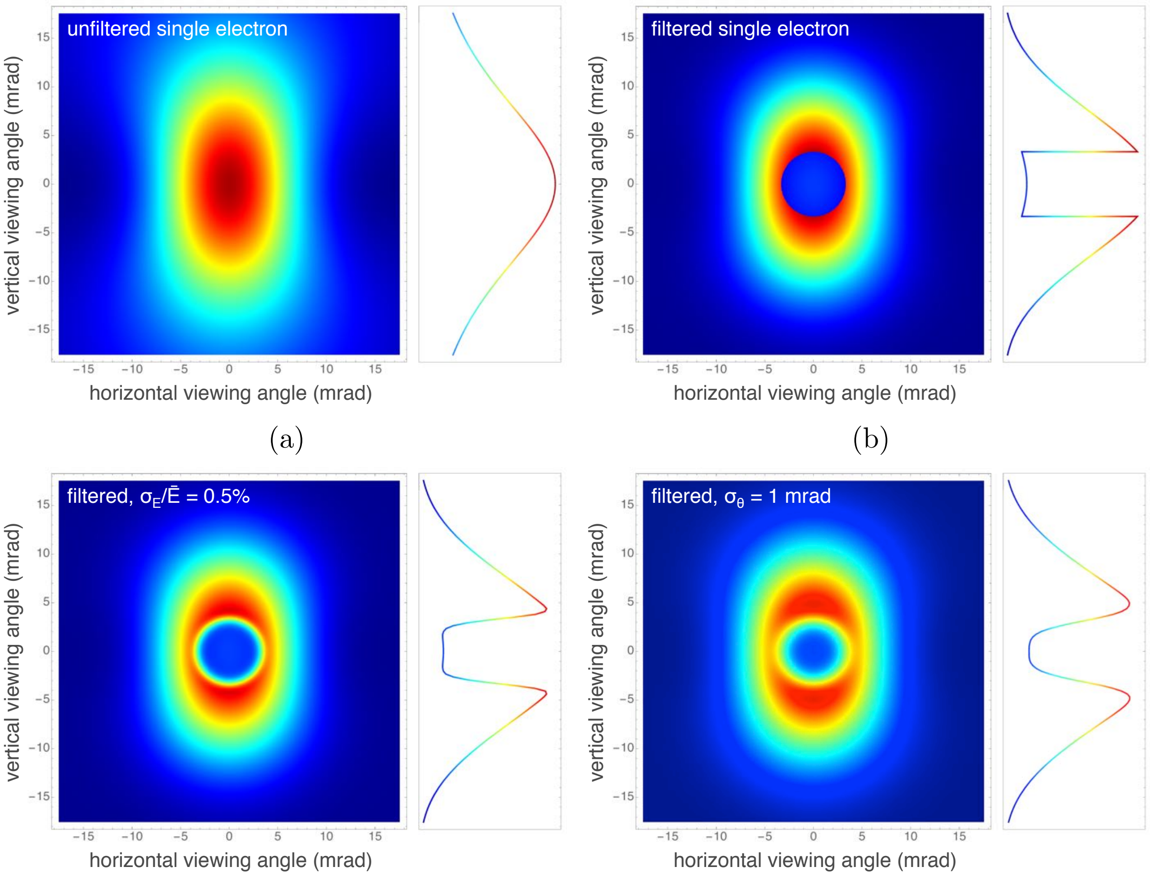

(a) (b) (c) (d)

Figure 5.4: (a) Compton scattering flux distribution and vertical profile through the center of a horizontally polarized 532-nm laser from a 29.1-MeV electron. (b) Flux distribution and vertical profile filtered with a 75-µm Sn foil, showing a K-edge hole. (c) Filtered flux distribution and vertical profile from a beam of electrons having 0.5% energy spread and no divergence. (d) Filtered flux distribution and vertical profile from a beam of electrons having 1-mrad divergence and no energy spread.

5.5, the effects of beam parameters on the vertical profile are clearly shown. Unsurprisingly, energy shift Δ_E causes the most quantifiable change by the difference in hole size. Edge blurring due to σ_E and σ_θ are more subtle, but there are important differences between the two. As mentioned before, divergence causes drastic spectral bandwidth changes along the viewing angle, while energy spread has more constant bandwidth throughout. This difference is clear when comparing the on-axis and off-axis changes. In the σ_θ case, the intensity in the central region remains unchanged as divergence increases due to the preservation of narrow spectrum in the on-axis region, but the off-axis region is blurred considerably. Conversely, in the σ_E case, the central region gets brighter when energy spread increases to 1%, indicating a presence of more low energy photons in that area, but off-axis region slopes stay sharper than that of the $\sigma_\theta = 1\,\text{mrad}$ case. The exact shape of the slope depends on the shape of the distribution in the beam's energy spread and divergence.

5.4 Experimental setup

5.4.1 Linear accelerator and interaction laser

The K-edge beam diagnostic was experimentally demonstrated using the 30-MeV X-band linear accelerator at LLNL. The accelerator was designed to produce high-brightness LCS X-rays by head-on collision with a 532-nm laser. The detailed parameters of the accelerator, laser and output X-rays are given in previous publications[42, 33, 34] and summarized in table 5.1. A layout of the laser-electron interaction region is shown in Fig. 5.6. The accelerated beam is focused by a quadrupole triplet just before the interaction point, where it collides head-on with the interaction laser and is bent by the spectrometer dipole to the beam dump. The energy spectrum was measured using the spectrometer, and emittance was measured using the quadrupole scanning method, showing good agreement with PARMELA design values[43, 44]. For this diagnostic experiment, the energy of the electron beam was tuned so that the LCS X-rays would produce a K-edge hole of adequate size given the choice of filter material and field-of-view. The interaction laser is linearly polarized in the horizontal direction.

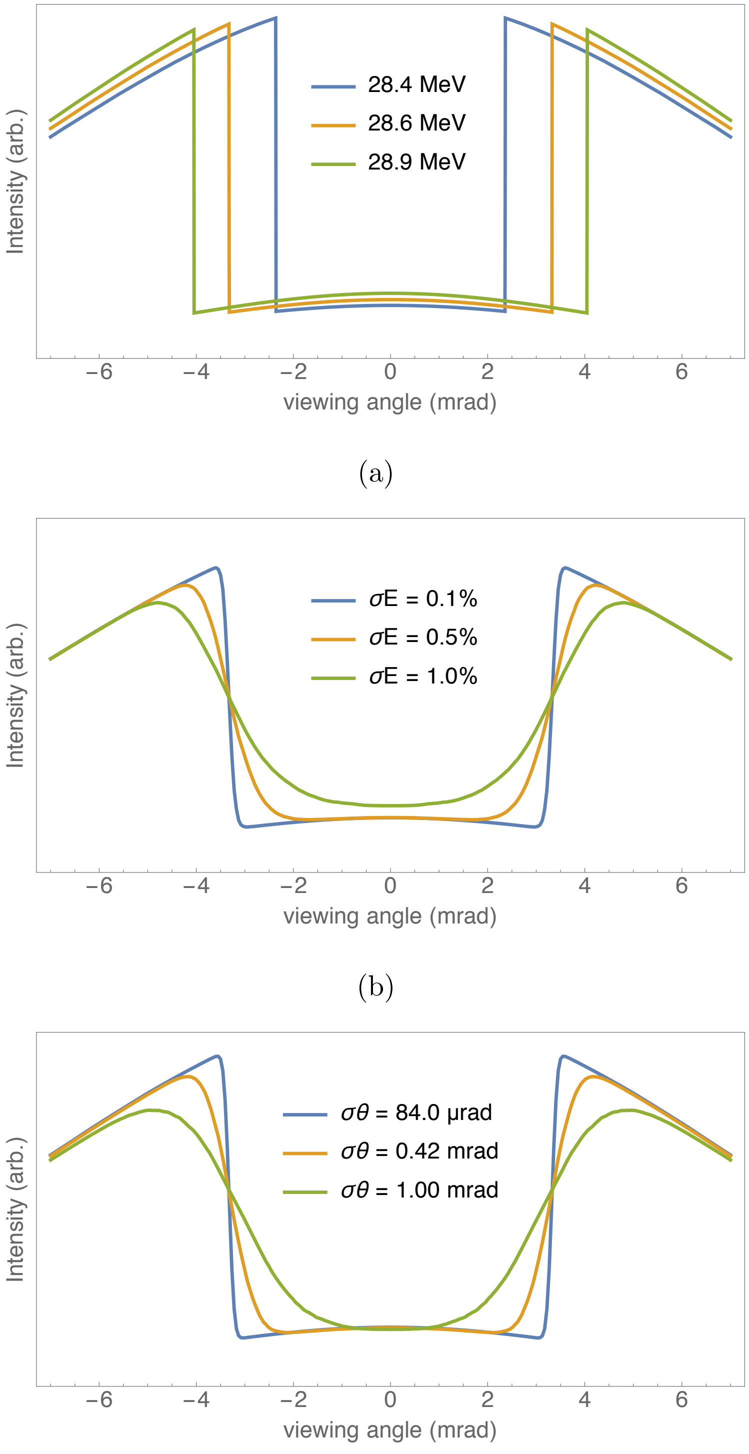

(a)

(b)

(c)

Figure 5.5: Effects of different beam parameters on the K-edge hole image vertical profile: varying energy (a), varying energy spread (b) and varying divergence (c).

5.4.2 LCS X-rays

The Compton-scattered X-ray beam has a maximum energy of about 30 keV, with $1/\gamma$ divergence of 17 mrad. From the interaction region, it travels forward and passes through a 45° mirror used to direct the laser beam to the interaction region. The original thickness of the fused silica mirror is 9.525 mm, which would absorb nearly all of 30-keV X-rays. In order to make it possible to image the X-rays, a 20.32-mm diameter region of the mirror in its center was thinned from the back to have a 2-mm thickness. Since the mirror is positioned at 45°, the X-rays penetrate through 2.828-mm of fused silica and are attenuated by about 40%; the angled position also causes this aperture region to be football-shaped when imaged. The mirror is placed 1.4 m downstream of the interaction region, giving the apertured field-of-view of 14 mrad long and 6 mrad wide. After the mirror, the X-ray beam exits the vacuum chamber via a 435 µm-thick Be window.

The X-rays are then filtered by the K-edge foil. For 30-keV X-rays, Sn foil was used as demonstrated in section 5.3.1. For lower energies, In (27.9 keV) and Ag (25.5 keV) were used as well. The thickness of the filters were chosen to maximize the absorption difference between above and below the K-edge. For Sn, the ideal thickness is 65 µm at which the difference in absorption would be 56.6 percentage points (87.6% absorbed above K-edge, 31.0% absorbed below K-edge); 75 µm was used as it was the closest thickness available for purchase, with 56.1 percentage point difference in absorption. The filtered X-rays were imaged 1.2 m further downstream with Fujifilm imaging plates and Andor image-intensified CCD cameras coupled with either a CsI scintillator or a P43 (Gd_2O_2S:Tb) phosphor screen. Since the CCD camera gives real-time information, it was used to monitor the centering of the X-ray beam on the aperture by steering the electron beam. However, due to an issue regarding non-uniform response across the imaging area for the CCD camera, only imaging plate data were used for analysis. The imaging plates were scanned using Fujifilm FLA-7000 within 15 minutes of the conclusion of exposure. Typical exposure lasted 20-30 minutes, corresponding to accumulation of about 12,000-18,000 shots.

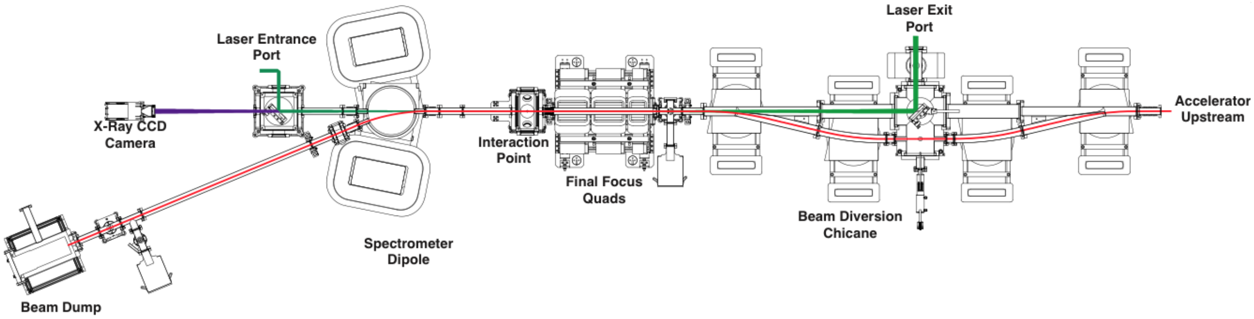

Figure 5.6: Layout of the LLNL Laser-Compton Light Source interaction region and its surroundings. Electron beam path is shown in red, laser in green and X-rays in purple.

Table 5.1: LLNL LCS source parameters

e^- beam parameters		laser, X-ray parameters	
bunch charge	100 pC	laser energy	750 mJ
bunch length	2 ps	pulse length	6.5 ns
spot size	30 µm	beam waist	50 µm
n. emittance	0.3 µm	wavelength	532 nm
RF	11.424 GHz	X-ray energy	30 keV
energy	30 MeV	X-ray flux	3×10^6/s
energy spread	0.03 %	rep. rate	10 Hz

5.5 Laser-Compton X-ray Modeling

All of the spectral and imaging simulations were done using a Mathematica script originally written by F. V. Hartemann and S. Wu for LCS optimization and modified by P-C. Yeh and Y. Hwang. The code calculates the Compton scattering cross section and flux for a model electron beam (a collection of particles input from PARMELA) and a laser pulse modeled as a plane wave field with a Gaussian beam envelope. The original PARMELA particles' phase space values were modified to create electron beams with desired beam parameters.

In the code's coordinate system, the laser pulse is traveling along the z axis. Since it is modeled as a perfect plane wave with only intensity variations given by the Gaussian beam envelope, laser bandwidth and divergence effects are not taken into account. A spatial grid based on observation angles θ_x and θ_y, corresponding to horizontal and vertical polar angles from the axis respectively, serves as the 2D pixel grid. At each grid point and for each electron particle, the Compton scattered energy and differential cross section is calculated using energy-momentum conservation and the Klein-Nishina formula for linearly polarized photons[10]. The interaction probability of the electron particle with the laser beam is calculated by integrating the photon density along the ballistic trajectory of the electron, and is multiplied to the cross section to give the number of photons per solid angle for the grid point. This process is repeated for all grid points and electron particles, and the contribution from each electron particle is summed for final image.

The aperture created by the back-thinned optic was modeled by multiplying the cross section by the fused silica transmission coefficient with thickness depending on the expected penetration length determined from the electron particle position and the imaging grid point. Other filtration effects due to K-edge foil and Be window were calculated by simply multiplying the transmission coefficient of respective material without added spatial complexity since the thickness is considered uniform for all X-rays. Response of the imaging modality was modeled using the absorption coefficient of respective scintillation material multiplied by the X-ray energy.

5.6 Results and analysis

A 30-minute (18,000 shot) integration image of unfiltered X-rays captured with an imaging plate, along with a simulation of the image are shown on Fig. 5.7. The horizontal and vertical profile lineouts through the center are also plotted, showing excellent agreement of intensity distribution apertured by the back-thinned optic between the experimental data and modeling.

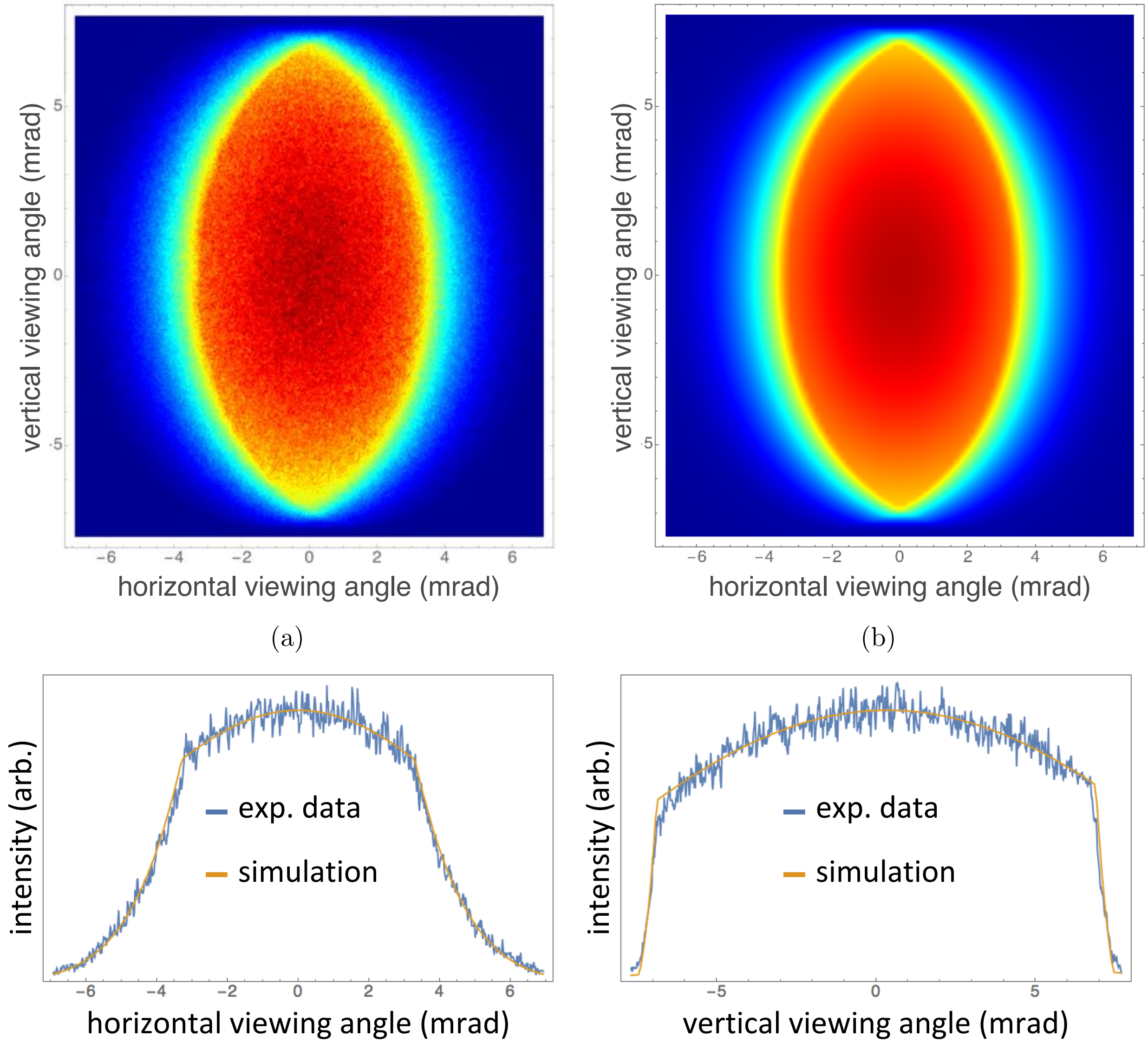

(a)

(b)

(c)

(d)

Figure 5.7: Image of unfiltered X-rays, apertured by the back-thinned optic (a), simulation of the unfiltered X-ray image (b), horizontal (c) and vertical (d) lineouts of the image and simulation through the center.

A Sn-filtered X-ray image, also integrated for 30 minutes, is shown on Fig. 5.8, and its vertical lineout through the center and simulation fits made with varying beam parameters are shown on Fig. 5.9. The simulations were normalized to have same intensity as the experimental data at the center and at the edges, thus easily visualizing how well the simulations fit near the shoulders for different parameters. The best fit parameters for this image were

$\bar{E} = 28.51\,\mathrm{MeV}$, $\sigma_\theta = 1.8\,\mathrm{mrad}$, and $\sigma_E/\bar{E} = 0.07\%$.

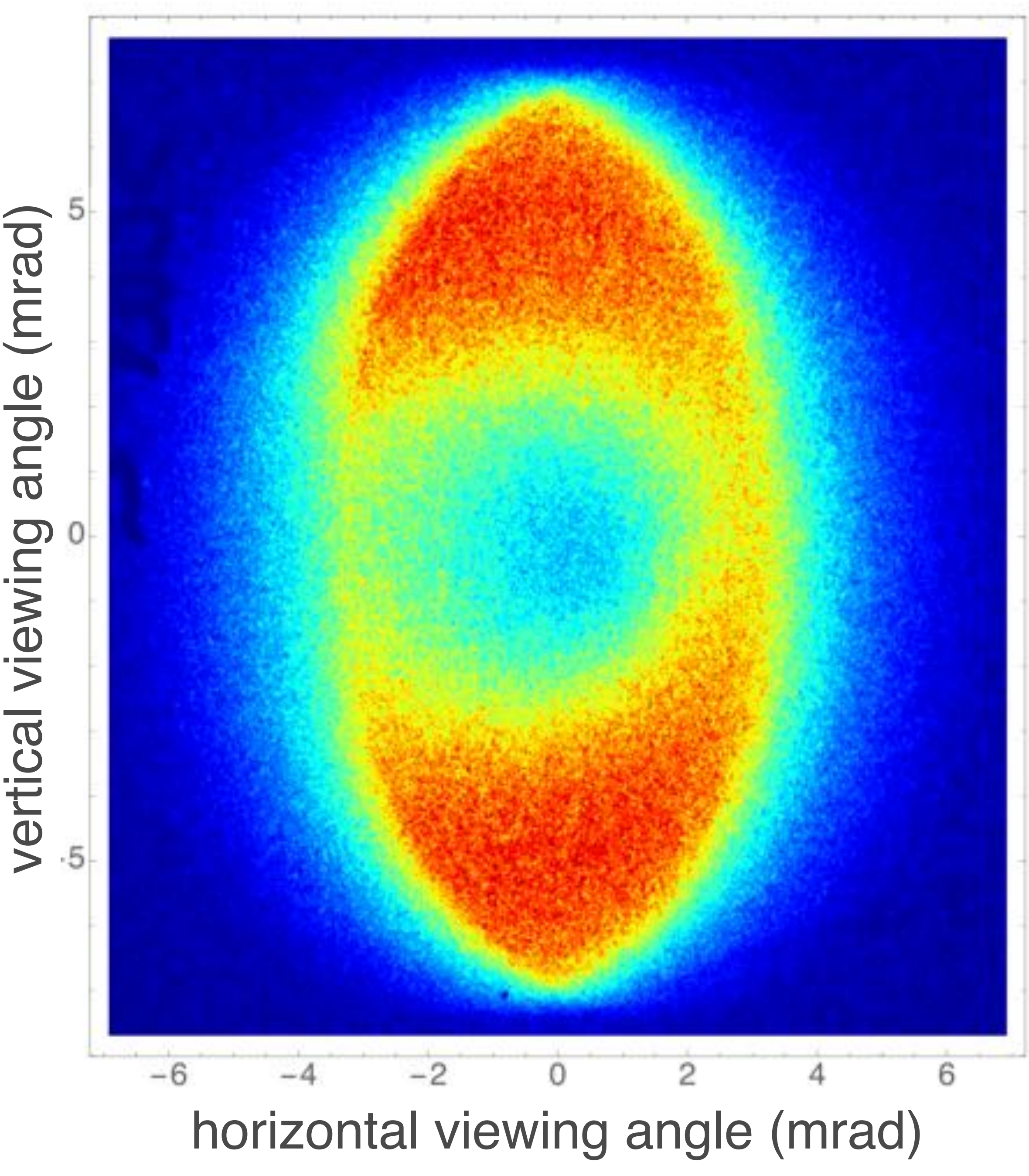

Figure 5.8: Sn-filtered LCS X-ray image, showing the K-edge hole in the center.

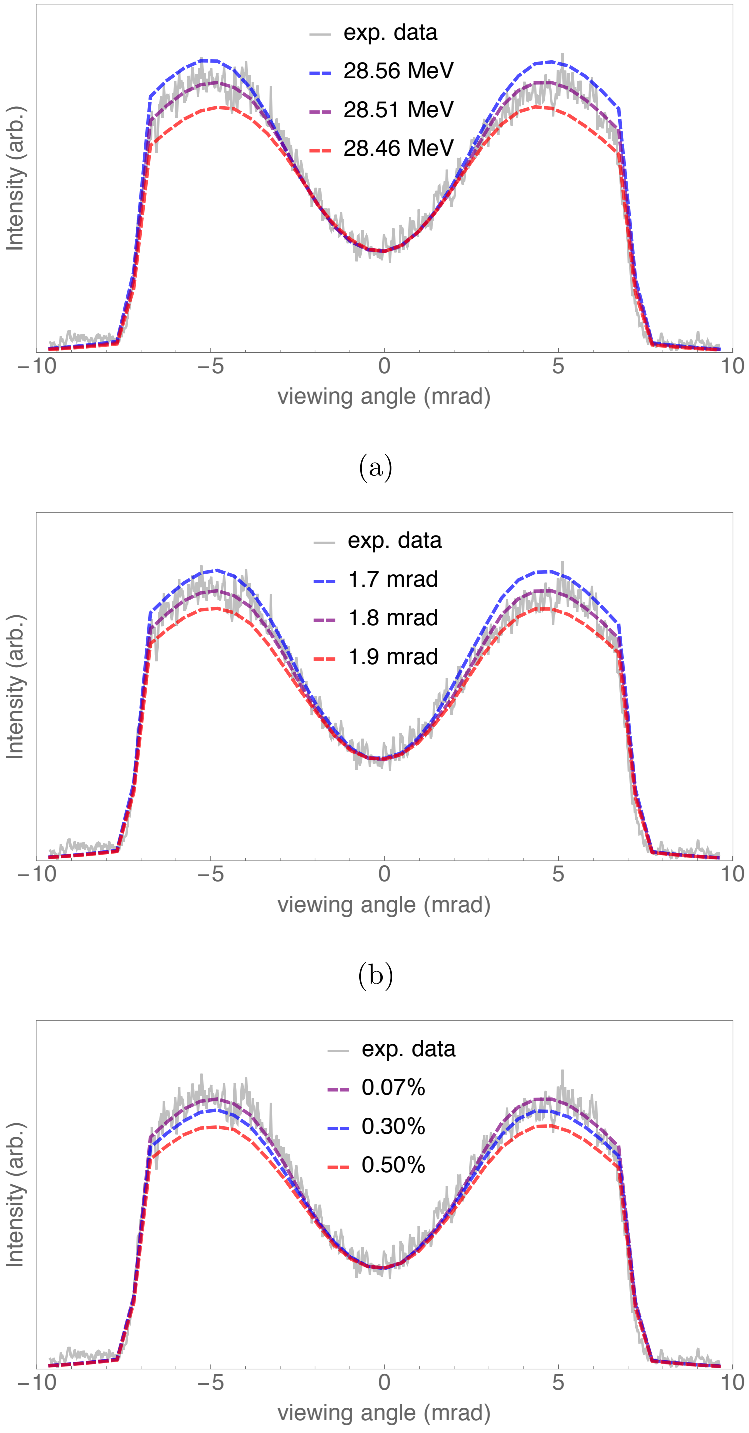

(a)

(b)

(c)

Figure 5.9: Effects of different beam parameters on the K-edge hole image vertical profile: varying energy (a), varying energy spread (b) and varying divergence (c). Upper/lower bound fit errors are shown in different colors.

5.6.1 Mean energy

As shown in Fig. 5.9a, the K-edge profile is very sensitive to the mean energy of the electron beam. The red and blue lines represent less than ±0.2% error in energy from best fit, plotted in purple. As expected from the ideal beam case (Fig. 5.5a), the size of the hole, measured as peak-to-peak distance, changes considerably. This method revealed a more precise measurement of energy than the spectrometer measurement where magnetic field probe calibration and angle measurement uncertainties prohibit high precision.

5.6.2 Divergence

The precision for divergence measurement is shown in Fig. 5.9b. Red and blue lines represent 6% error from the best fit of 1.8 mrad. Although single-shot normalized emittance of 0.3 mm mrad and 30-µm spot size implies a divergence of about 0.2 mrad, The accumulation of 18,000 shots over 30 minutes seems to have introduced almost an order of magnitude higher jitter/drift contributions to the divergence. Possibility of the beam being energy spread-dominated with low divergence has been ruled out, as it was impossible to reproduce the exact shape with such parameters. Specifically, the profiles of high energy-spread simulations feature a flatter central trough, as explained in section 5.3.1 and Fig. 5.5.

5.6.3 Energy spread

Figure 5.9c shows the effect of changing energy spread, from nominal 0.07% in purple to 0.5% in red. Since the beam is heavily divergence-dominated, changing the energy spread value did not contribute to the off-axis spectral broadening and therefore the slope of the lineout stays unchanged within the plausible range determined from the independently measured single-shot energy spread 0.03% and jitter 0.06%. Therefore, it was only possible to give an upper bound for the energy spread at about 0.3%.

5.6.4 Applicability of the method

In this demonstration of the K-edge diagnostic, the low X-ray yield owing to the long-pulse interaction laser necessitated a half hour integration in order to obtain a clear image, and negatively affected the beam divergence measurement. This method would be most ideal for measuring the single shot beam emittance of laser wakefield accelerator beams, as such facilities already possess high-intensity lasers capable of producing bright LCS X-rays and divergence measurement options are limited[27]. The energy spectrum as measured from the dipole spectrometer supplies the spectral broadening contribution due to the energy spread, so simulating the X-rays only requires making ansatz divergence distributions. It should be noted that high intensity lasers commonly used to drive plasma wakefield will introduce nonlinear effects that also contribute to spectral broadening and must be accounted for in the simulations. The choice of filter material should be made based on the energy range of the electron beam and the laser wavelength; since there is an upper limit on atomic absorption edges – Pu K-edge is 121 keV – if the electron beam energy is too high, the LCS X-ray energy can be lowered by using a longer wavelength laser or reducing the interaction angle. Additionally, in cases where both electron beam energy and divergence are high enough that $1/\gamma$ divergence of the LCS X-rays is smaller than the beam divergence, the K-edge hole would be very difficult to image. Therefore, this method is best suited for energies below 100 MeV, where the LCS divergence would be wide enough for imaging the hole and filter materials are commonly available.

5.7 Conclusion

A diagnostic method that can determine electron beam's energy spectrum and divergence using K-edge filter imaging of LCS X-rays has been developed and tested on the X-band linear accelerator at LLNL. K-edge foils act as low-pass filters attenuating most of X-rays above the K-edge energy; the LCS spectral broadening due to beam divergence and energy spread are rendered as a gradual slope from dark, high energy region in the center to bright low energy region off-axis. By finding the beam parameters that fit the shape of the slope, one can determine the mean energy, energy spread and divergence. The 30-keV LCS X-rays were filtered with 29.2-keV Sn K-edge foil, and was able to find the mean energy and divergence with high precision. Because the spectral broadening was dominated by the divergence, only an upper limit for the energy spread could be obtained. Due to the precise divergence measurement capability, this method can be a very simple yet useful emittance measurement tool when combined with a spot size measurement for moderate energy electron beams.

Chapter 6

Medical Applications of Laser-Compton X-ray Sources

6.1 Introduction

Medical imaging and therapy has seen great advancements since the advent of synchrotron radiation (SR), utilizing its bright, monochromatic and tunable X-ray beam of very small source size[62]. However, medically relevant X-ray energies (keV to MeV) can only be obtained with GeV-class accelerators, mostly through undulator radiation. Such facilities are too large and costly, limiting the accessibility of SR radiology and radiotherapy. Therefore, a compact X-ray source that produces SR-like beam will provide a huge boost and aid in popularization of medical applications of SR.

X-ray and γ-ray generation by laser-Compton scattering (LCS) is being studied worldwide for its potential as a compact synchrotron-quality X-ray source[52, 38, 21, 70, 40]. LCS can be seen as SR with the undulator replaced by the laser's electric field, therefore shortening the scattered photon frequency by more than 3 orders of magnitude. In a head-on collision of a laser and an electron beam, photons backscattered in the electron beam direction gain energy up to a factor of $4\gamma^2$, where γ is the electron beam Lorentz factor. Using optical lasers, hard X-rays in the range of 10-100 keV can be produced with electron linear accelerators with energies less than 50 MeV. Such accelerators are commonly used in hospitals for external beam therapy. Hence, LCS can provide a breakthrough in medical imaging and therapy by introducing SR to every hospital. In the following, notable medical SR applications are discussed and its feasibility study plan using the LLNL Compact Laser-Compton X-ray Source is presented.

6.2 Medical imaging with LCS

Conventional radiology relies on Bremsstrahlung X-rays produced by an electron beam of tens of keV hitting an anode target. It is very compact and simple to operate, but due to its broad spectrum the patient receives unnecessary dose from low-energy X-rays which also reduces the quality of the image especially in the case of computed tomography (CT) due to beam hardening. One may use a filter material to block the low-energy portion or use a target possessing a specific fluorescent radiation peak, at the loss of overall flux. In contrast, a monochromatic beam as in the case of SR or LCS can significantly reduce the patient dose while improving the resolution of the image. Monochromatic beams can also provide a much higher contrast for contrast agent imaging if the contrast agent's K-edge is just below the beam energy.

6.2.1 K-edge Subtraction Imaging

The energy tunability of LCS, in the form of ether direct change in electron beam energy, different colored laser, change in interaction angle or change in observation angle, enables a new imaging technique known as K-edge subtraction (KES). In this scheme, an image with X-ray energy just above the K-edge of the contrast agent is subtracted from a similar image but with the X-ray energy just below the K-edge. Since the attenuation coefficient of body parts not containing the contrast agent are nearly constant between the two energies as shown in Fig. 6.1, these features are completely subtracted and only the contrast agent image remains.

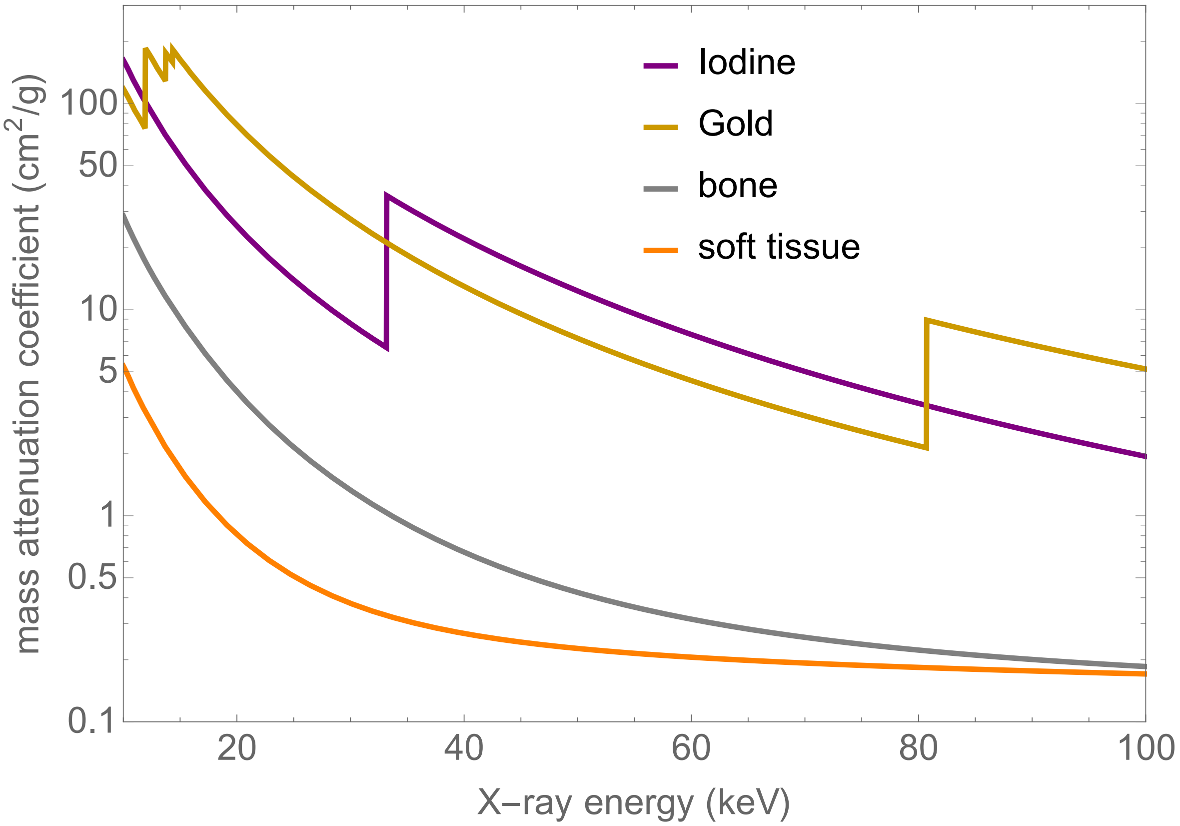

Figure 6.1: Mass attenuation coefficients for body tissues and contrast agents.

6.2.2 Phase Contrast Imaging

For hard X-rays in body-like matter, the real part of the refractive index is larger than the imaginary part, causing bigger changes in phase than in absorption. The phase change in matter can be detected in a number of ways. With a spatially coherent beam one can observe directly the refractive edge-enhancement effect[68]. With a monochromatic beam, X-ray diffraction can be used to detect the small angle refractions of the beam[19]. Further, various interferometric methods have been used to extract detailed phase shift information[11, 67]. These techniques have been successfully demonstrated using LCS by Bech et al.[8].

6.3 Radiotherapy with LCS

Current X-ray radiotherapy is mostly carried out using MeV beams created from medical linacs or characteristic γ-rays from radioisotopes, but there is a new technique using <100 keV beam to trigger Auger cascade of high-Z nanoparticles placed near cancer cells[54]. Nanoparticles accumulate in tumors due to the enhanced permeability and retention (EPR) effect, where abnormal blood vessel structures in tumors allow macromolecules to permeate more readily and be retained longer than in normal tissues. Selectivity can be further increased by attaching tumor targeting molecules to the surface of the nanoparticles. Furthermore, the nanoparticles can serve as contrast agents as well as a radiosensitizer as in image-guided radiotherapy (IGRT)[30], enabling diagnostics and therapy to be performed with the same beam and drug, also known as theranostics. Combined with the monochromaticity of LCS, the dose selectivity can be greatly increased.

In order to study the viability of LCS in Auger theranostics, nanoparticles and biological samples including live cells are required. If active cancer-targeting agents are to be loaded to the nanoparticles, a comparison study of cancer cells and living cells can be made in a similar fashion. If one only relies on the passive EPR effect, a live animal will be required to grow the vascular structures for the tumor. Gold is the favored nanomaterial most widely studied for Auger radiosensitization, and it has been shown that the X-ray beam need not be above the Au K-edge in order to see the enhancement effect[45].

6.3.1 Monte Carlo simulation of nanoparticle Auger therapy

FLUKA[22] simulations of dose distribution in a Gadolinium Auger therapy were done assuming a monochromatic beam. In order to maximize the K-edge dose, the energy was set to 60 keV, near the Gd K-edge of 50.3 keV. A pencil beam of monochromatic X-rays impinged on a 1-nm sphere of solid-density Gd surrounded by water to study the Auger electrons' dose distribution in the nm range. The 2-dimensional dose distribution was scored along a 10-µm long and 1-µm wide box region, and is shown in Fig. 6.2.

It is clear that most of the dose absorption occurs along the X-ray path within the 1-nm Gd sphere, as expected. The slight halo around the sphere represents the dose due to secondary particles, and since low-energy Auger electrons dominate, the halo has a very short range on the order of 50 nm. Figure 6.3 shows the comparison of how much dose enhancement is to be expected, with slice dose distributions at $z = 0$ µm, where the Gd sphere is located, and at $z = 1$ µm where the dose is mostly from the primary X-rays. It is clearly seen that the region where dose is higher than the region directly irradiated by primary X-rays extends to about 50-100 nm. The result implies that if a delivery agent can transport high-Z atoms inside the nucleus, there will be a direct dose enhancement to the DNA. The radiobiolgical effects of such highly localized dose, whether inside or outside the nucleus, needs to be investigated further.

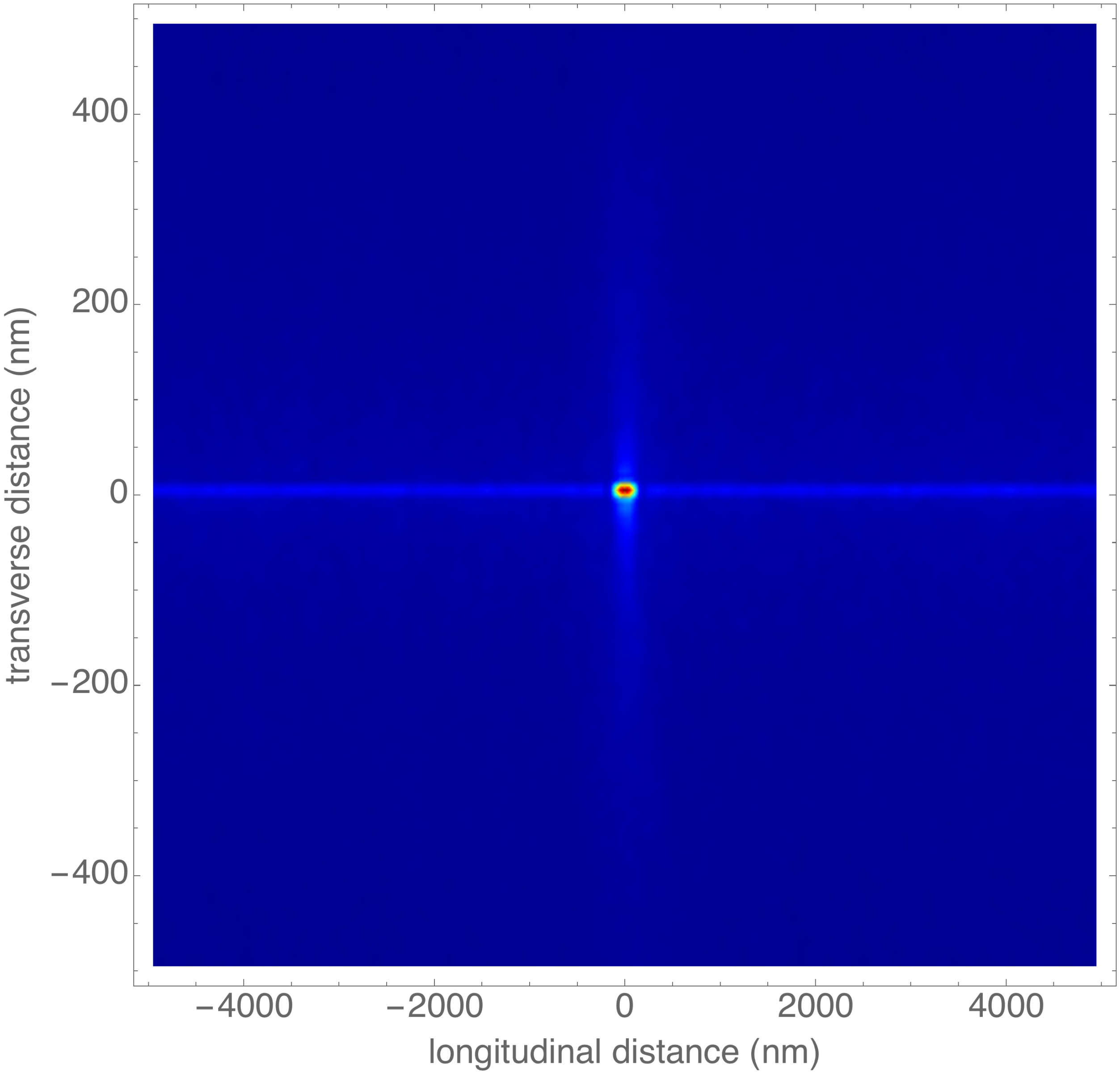

Figure 6.2: Dose distribution near a 1 nm radius Gd sphere hit by 60 keV X-rays.

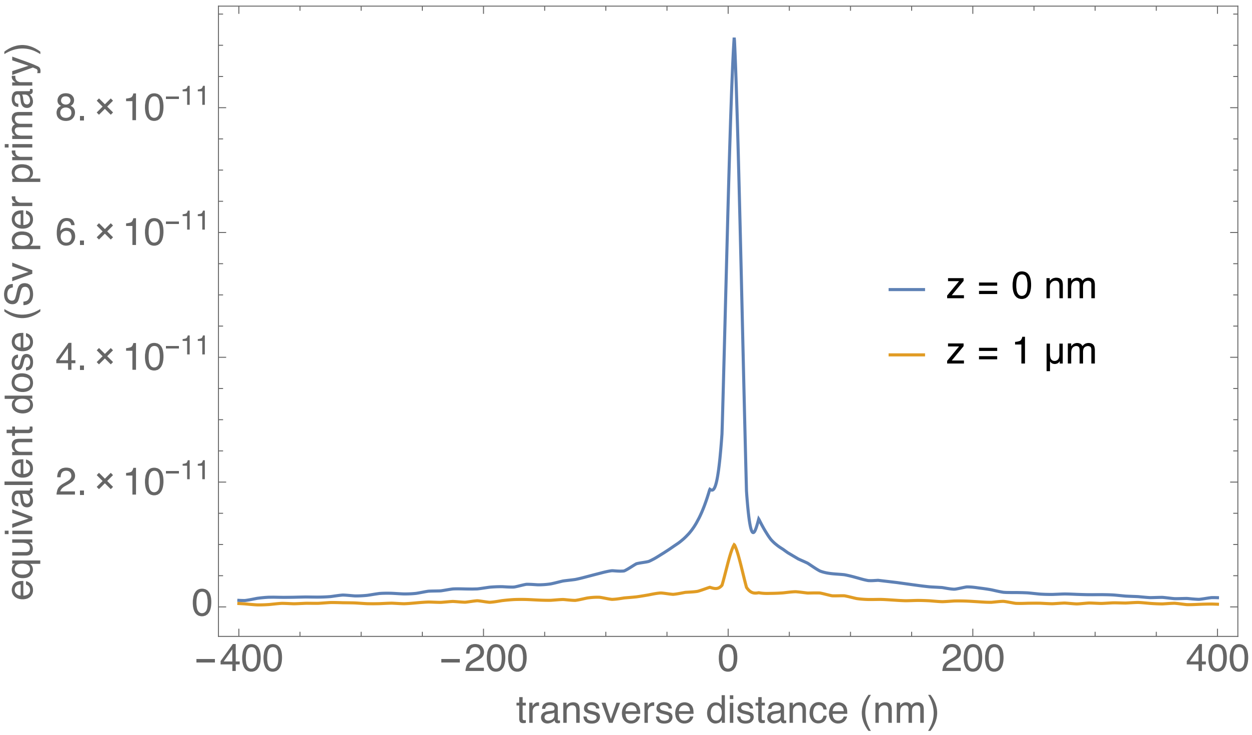

Figure 6.3: Dose distribution near a Gd sphere hit by 60 keV X-rays

Chapter 7

Boron Neutron Capture Therapy

7.1 Introduction

Neutron capture therapy is a field of external beam radiotherapy where a material of high neutron capture cross section is inserted into the body near the tumor, and the patient is subsequently irradiated with a neutron beam which activates the highly absorbent atoms to produce local ionizing radiation. Boron-10 is the most widely studied material for neutron capture therapy; once it captures a neutron it splits into a Li ion and an α particle of few MeV. These ions have mean free path of less than 10 µm, depositing huge dose mostly within the volume of the cell the Boron atom was originally located in. Since thermal neutrons have very low absorption cross section for atoms that consist the body compared to Boron-10, the dose localization can be very high. However, the lack of suitable neutron source – nuclear fission reactors are typically where neutron capture therapy are performed – and a Boron delivery method that has high tumor-to-body discrimination ratio has limited the applicability of Boron neutron capture therapy (BNCT). Recent development of accelerator-based neutron sources enable compact BNCT facilities, and new Boron carriers such as nanoparticles that achieve higher than 10:1 contrast ratio can drastically enhance the local dose ratio. Therefore, FLUKA[22] was used to simulate new regimes of BNCT. The dose distributions were investigated for 3 distinct cases: macroscopic dose distribution in a medium with homogeneous Boron-10 concentration, macroscopic dose distribution in a medium with a region containing 10 times higher Boron concentration, and microscopic dose distribution within a model of a cell. The first simulation was accompanied with a scan of neutron beam energies in order to investigate the dependence of depth of maximum dose distribution as a function of incident energy. It was found that for energies below 10 keV, the dose is mostly limited to the first couple centimeters, given a concentration of 100 ng of Boron-10 in mg of water. The the second simulation, a 1-keV beam was used to penetrate through 5 cm of target where a tumor model was located containing a 10x concentration of Boron compared to its surroundings. Various concentrations of Boron-10, while maintaining the 10:1 ratio, were simulated and found that the optimal concentration is around 100 ng ^{10}B/ mg H_2O in order to minimize the dose in the front of tumor. Lastly, a cell model where a 10 nm thick sheath of Boron-10 is surrounding a 3 µm-radius nucleus was created to determine the amount of dose deposited as a function of distance from the center of the nucleus. As the dose is delivered by α particles and Li ions of energy on the order of 1 MeV, which deposit most of their dose within 6 µm, the dose is largely localized to the nucleus, increasing the effectiveness. It was found that 48% of the total dose is delivered to within the nucleus.

7.2 Energy dependence of macroscopic dose distribution in homogenous target

The energy of the incident neutron beam is an important factor of consideration, as the Boron neutron capture cross section is heavily dependent on the neutron energy. In the following simulations, a mixture of Boron-10 and water with a concentration of 100 ng ^{10}B/ mg H_2O

was used as the target. Thermal energy neutron beam is almost entirely absorbed in the first centimeter, depositing peak dose at the entrance and rapidly decreasing as a function of distance. At higher energies, neutrons have lower cross sections, and those that have not interacted with a Boron will slow down as they travel through water, thereby increasing the chance of capture. This mechanism results in a peaking dose profile deeper in the water. The peak shifts from 5 mm at 100 meV to 3 cm at 10 keV.

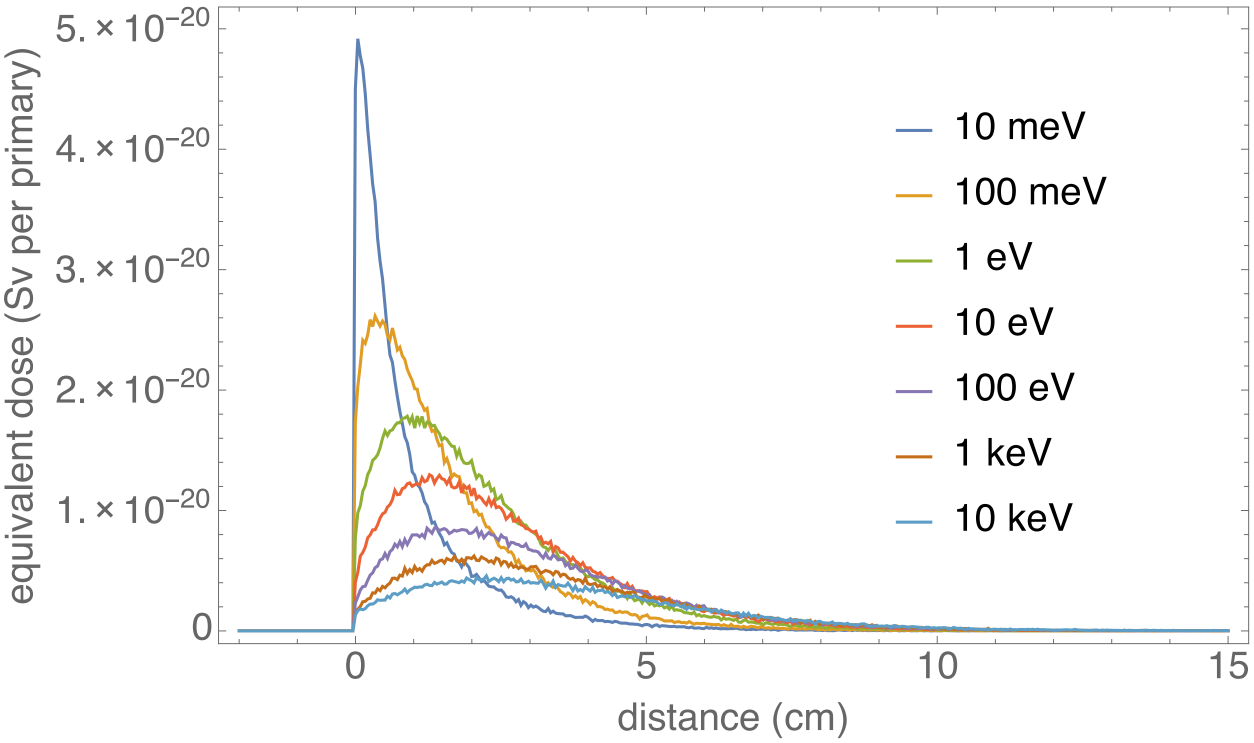

Figure 7.1: Energy dependence of BNCT dose distribution

7.3 Macroscopic dose dependence on Boron-10 concentration

A 1-cm long tumor region seated 5-cm deep was simulated to find the macroscopic dose distribution. The neutron beam energy used was 1 keV. Boron-10 was distributed in the tumor region at a concentration of 10-10,000 ng ^{10}B/ mg H_2O, with rest being water. The surrounding body was given 10 times less Boron distribution compared to the tumor region to maintain a 10:1 ratio. The neutrons are mostly absorbed in the first 2 cm of skin, depositing maximum dose at 2-cm depth before falling quickly until the 10x higher Boron concentration is encountered. The ratio of the peak dose between the 2-cm depth and tumor is affected by the Boron concentration. At low concentrations, the dose at the front of the tumor is about double the peak dose at skin. As the concentration increases to 1 µg ^{10}B/ mg H_2O, the skin dose peak increases relative to the tumor dose, and at 10 µg ^{10}B/ mg H_2O the skin peak dose is 1.5 times the tumor dose. Furthermore, because the higher concentration directly leads to less neutrons penetrating all the way to the tumor, the increase in dose is not linearly proportional to the concentration; the total energy deposited at tumor is roughly the same for 1 µg ^{10}B/ mg H_2O and 10 µg ^{10}B/ mg H_2O and only 100 times more than 10 ng ^{10}B/ mg H_2O. Based on these results, the optimal concentration of 10:1 contrast ratio Boron-10 for a tumor seated 5 cm deep is around 100 ng ^{10}B/ mg H_2O.

7.4 Microscopic dose distribution

A model of a cancer cell with Boron nanoparticles attached to the surface of its nucleus was modeled as a 3-µm radius sphere and a 10-nm thick sheath surrounding the sphere, containing 10% Boron and 90% water. Modeling the cell as a 10-µm cube, this simulations Boron concentration corresponds to about 113 ng ^{10}B/ mg H_2O. As seen in the slice of dose distribution in Fig. 7.3, most of the dose is concentrated around the Boron shell. The total dose inside the nucleus is nearly equal to the dose outside of it. A dose profile per unit volume as a function of radial distance from the center of the nucleus is plotted in Fig. 7.4, with the nucleus boundary marked in red.

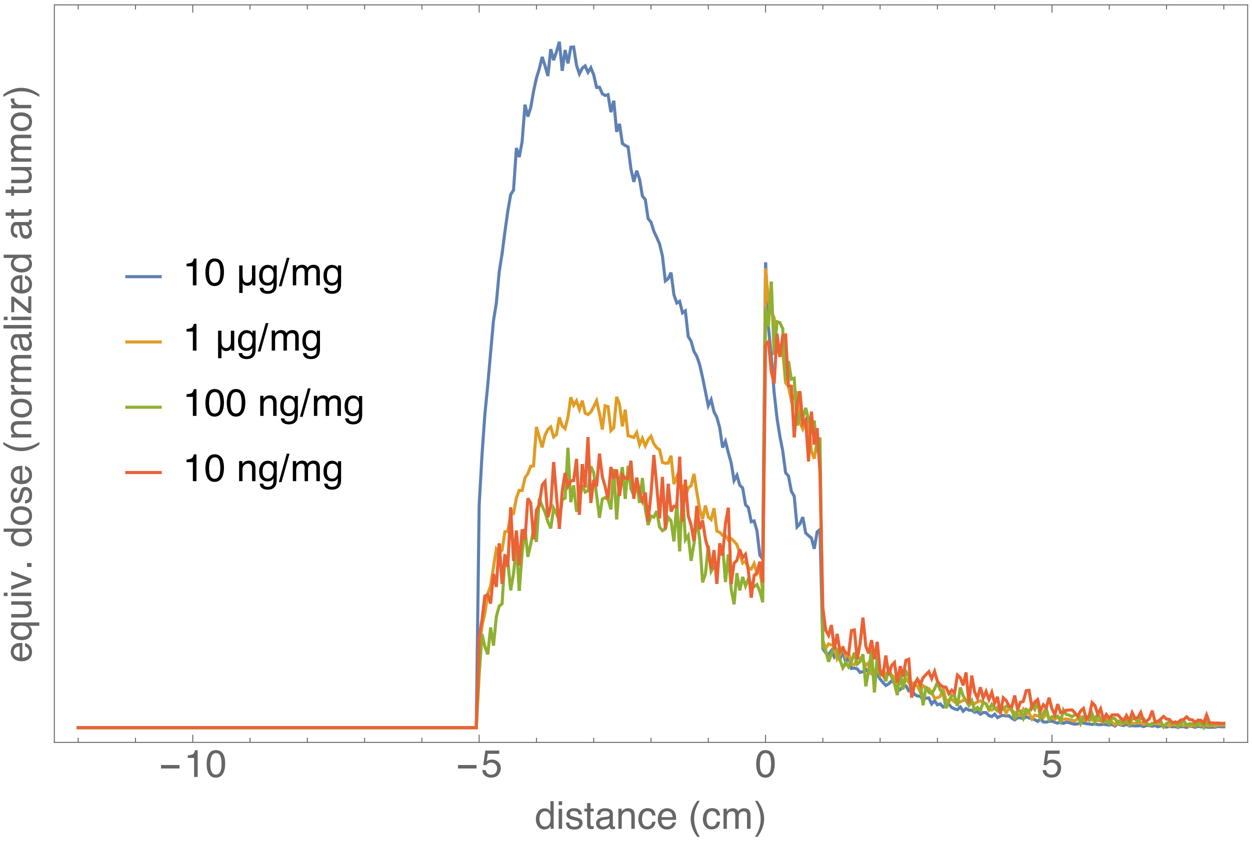

Figure 7.2: Boron concentration dependence of dose distribution

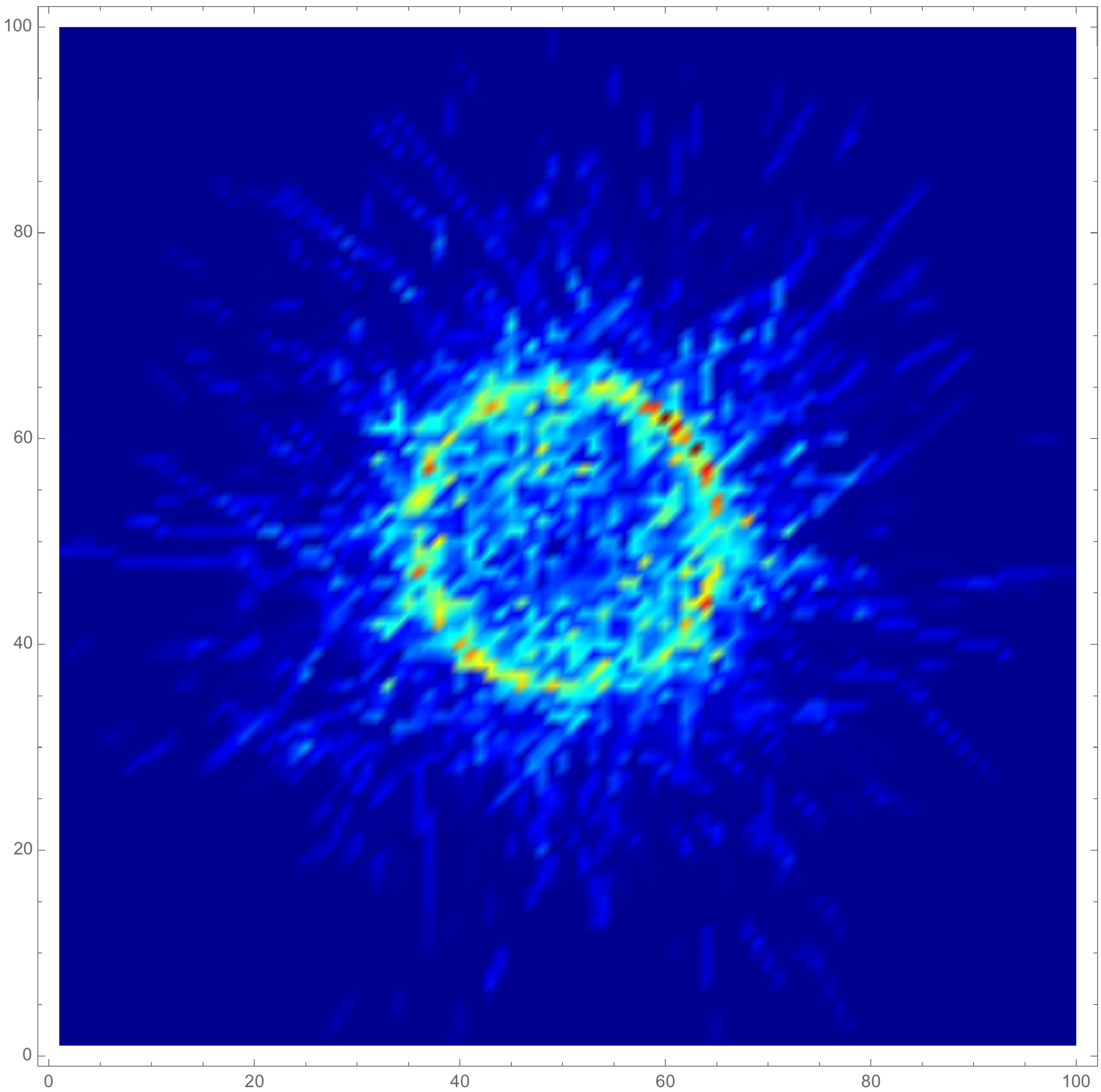

Figure 7.3: cross section of dose profile through the center of nucleus

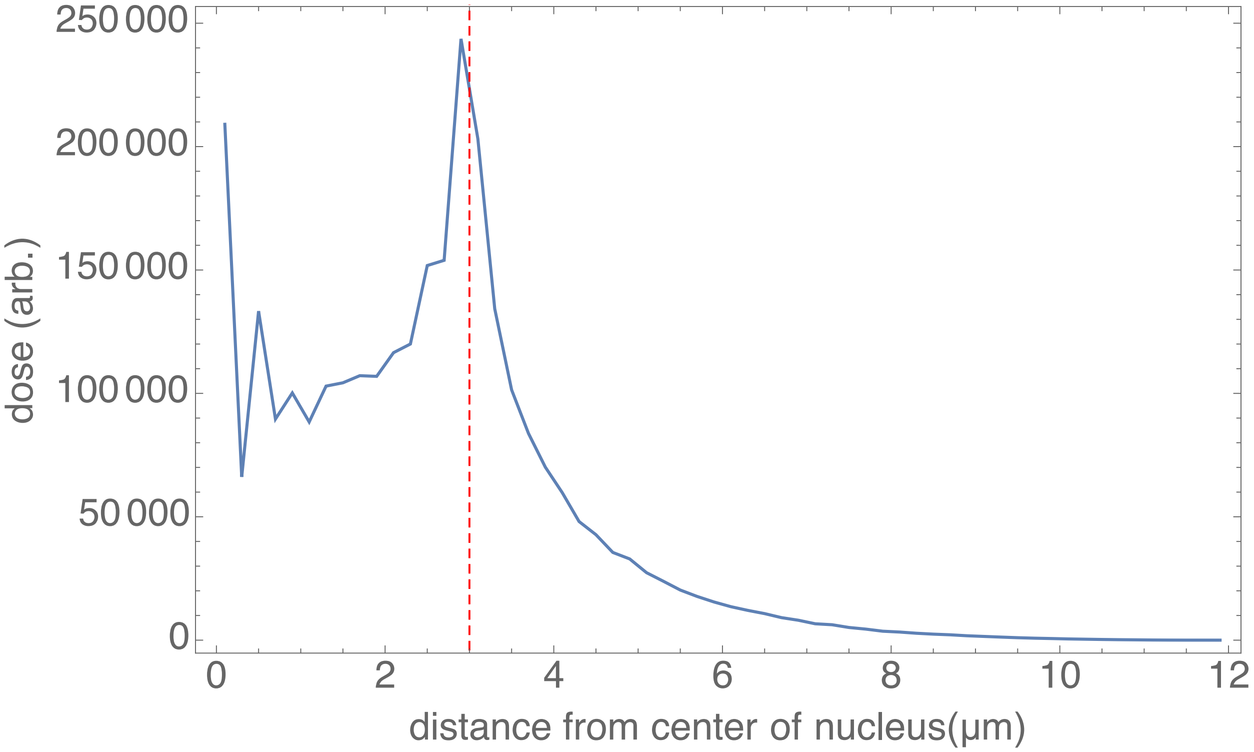

Figure 7.4: Radial distribution of dose per volume

Chapter 8

Conclusion and future outlook

8.1 Characterization of electron beam and X-rays

The electron beam and X-ray parameters of the LLNL Compact Laser-Compton X-ray Source have been measured and compared against theoretical models. The energy spectrum of the electron beam was measured using the dipole spectrometer, and the RMS spread was 0.031% with an RMS jitter of 0.061%. The transverse beam size at the interaction point was measured with OTR images. With the tightest focus, the RMS spot size was 14.4 µm × 11.0 µm with an RMS jitter of 5.11 µm × 2.77 µm. The transverse emittance was measured with the quadrupole scan method using the quadrupole triplets after the accelerating section and a YAG screen 1 m downstream. The normalized emittance was 0.3 mm-mrad at 80 pC.

The X-ray energy was inferred using a K-edge foil at various energies, from Silver (25.5 keV) to Tin (29.2 keV). The flux was measured using a calibrated scintillator-based X-ray CCD camera and yielded the expected value of on the order of 10^5 photons per shot. The source size was measured using a test pattern, and after accounting for the camera's spatial resolution, the source size was determined to be no larger than 42 µm.

8.2 LCS K-edge foil electron beam diagnostic

Since the LCS X-ray spectrum is highly sensitive to the electron beam's divergence and energy spectrum, a method using a K-edge foil filter to infer the X-ray spectrum and by extension the electron beam parameters was devised and tested. The results showed that the method can be a very useful diagnostic for the mean energy and the beam parameter that dominates the X-ray spectral broadening; in the test case the beam divergence could be measured to 5% accuracy while the energy spread could not be determined due to extremely low spectral broadening contribution from the 0.06% energy spread of the electron beam. Since the preparation of the method only requires a laser to be scattered from the electron beam and a foil of the correct K-edge energy, it can be a simple yet powerful beam diagnostic method.

8.3 Medical applications of LCS

The potential of medical imaging and therapy with LCS X-ray sources are largely inspired from novel medical applications being developed for synchrotron radiation light sources that utilize their monochromaticity, energy tunability and small source size. Among them, high-Z material radiology and radiotherapy has a potential to carry out diagnostics and therapy in one setting with a single drug and irradiation method. The possibility and dose deposition profile of Gadolinium nanoparticle based therapy was simulated using a Monte Carlo code FLUKA. It is confirmed that the secondary particle dose enhancement is localized to less than 100 nm of the Gd atom. Cancer-seeking materials with high specificity for tumor, penetration into the cell nucleus and ability to carry high-Z atoms such as Gd can enable such theranostic approach. However, the relationship of physical dose in the 100-nm range in various areas of the cell to radiobiological effects needs to be studied further in order to quantify the enhancement to be expected from these treatments.

Bibliography

[1] F. Albert, S. G. Anderson, D. J. Gibson, C. A. Hagmann, M. S. Johnson, M. Messerly, V. Semenov, M. Y. Shverdin, B. Rusnak, A. M. Tremaine, F. V. Hartemann, C. W. Siders, D. P. McNabb, and C. P. J. Barty. Characterization and applications of a tunable, laser-based, mev-class compton-scattering γ-ray source. *Phys. Rev. ST Accel. Beams*, 13:070704, Jul 2010.

[2] R. Alley, D. Arnett, E. Bong, W. Colocho, J. Frisch, S. Horton-Smith, W. Inman, K. Jobe, T. Kotseroglou, D. McCormick, J. Nelson, M. Scheeff, S. Wagner, and M. Ross. A laser-based beam profile monitor for the slc/sld interaction region. *Nuclear Instruments and Methods in Physics Research Section A: Accelerators, Spectrometers, Detectors and Associated Equipment*, 379(3):363 – 365, 1996. Proceedings of the Sixth International Conference on Instrumentation for Experiments at e+ e- Colliders.

[3] S. Anderson, F. Albert, A. Bayramian, G. Beer, R. Bonanno, R. Cross, G. Deis, C. Ebbers, D. Gibson, F. Hartemann, T. Houck, R. Marsh, D. McNabb, M. Messerly, R. Scarpetti, M. Shverdin, C. Siders, S. Wu, C. Barty, C. Adolphsen, T. Chu, E. Jongewaard, Z. Li, C. Limborg, S. Tantawi, A. Vlieks, F. Wang, J. Wang, F. Zhou, and T. Raubenheimer. Velociraptor: An x-band photoinjector and linear accelerator for the production of mono-energetic -rays. *Nuclear Instruments and Methods in Physics Research Section A: Accelerators, Spectrometers, Detectors and Associated Equipment*, 657(1):140 – 149, 2011. X-Band Structures, Beam Dynamics and Sources Workshop (XB-10).

[4] V. N. Baier and V. A. Khoze. Determination of the transverse polarization of high-energy electrons. *Sov. J. Nucl. Phys.*, 9(2):238, 1969.

[5] V. Balakin, V. A. Alexandrov, A. Mikhailichenko, K. Flöttmann, F. Peters, G.-A. Voss, V. Bharadwaj, M. Halling, J. A. Holt, J. Buon, J. Jeanjean, F. LeDiberder, V. Lepeltier, P. Puzo, G. Heimlinger, R. Settles, U. Stierlin, H. Hayano, N. Ishihara, H. Nakayama, K. Oide, T. Shintake, Y. Takeuchi, N. Yamamoto, F. Bulos, D. Burke, R. Field, S. Hartman, R. Helm, J. Irwin, R. Iverson, S. Rokni, G. Roy, W. Spence, P. Tenenbaum, S. R. Wagner, D. Walz, and S. Williams. Focusing of submicron beams for tev-scale e^+e^- linear colliders. *Phys. Rev. Lett.*, 74:2479–2482, Mar 1995.

[6] C. P. J. Barty and F. V. Hartemann. T-rex: Thomson-radiated extreme x-rays moving x-ray science into the “nuclear” application space with thompson scattered photons. Interal Report UCRL-TR-206825, Lawrence Livermore National Laboratory, Sep 2004.

[7] M.-M. Bé, V. Chisté, C. Dulieu, E. Browne, V. Chechev, N. Kuzmenko, R. Helmer, A. Nichols, E. Schönfeld, and R. Dersch. *Table of Radionuclides*, volume 1 of *Monographie BIPM-5*. Bureau International des Poids et Mesures, Pavillon de Breteuil, F-92310 Sèvres, France, 2004.

[8] M. Bech, O. Bunk, C. David, R. Ruth, J. Rifkin, R. Loewen, R. Feidenhans'l, and F. Pfeiffer. Hard X-ray phase-contrast imaging with the Compact Light Source based on inverse Compton X-rays. *Journal of Synchrotron Radiation*, 16(1):43–47, Jan 2009.

[9] M. J. Berger, J. Hubbell, S. Seltzer, J. Chang, J. Coursey, R. Sukumar, D. Zucker, and K. Olsen. Xcom: photon cross sections database.

[10] G. Bhatt, H. Grotch, E. Kazes, and D. A. Owen. Relativistic spin-dependent compton scattering from electrons. *Phys. Rev. A*, 28:2195–2200, Oct 1983.

[11] U. Bonse and M. Hart. An xray interferometer. *Applied Physics Letters*, 6(8):155–156, 1965.

[12] A. Bravin, P. Coan, and P. Suortti. X-ray phase-contrast imaging: from pre-clinical applications towards clinics. *Physics in Medicine and Biology*, 58(1):R1, 2013.

[13] W. J. Brown, S. G. Anderson, C. P. J. Barty, S. M. Betts, R. Booth, J. K. Crane, R. R. Cross, D. N. Fittinghoff, D. J. Gibson, F. V. Hartemann, E. P. Hartouni, J. Kuba, G. P. Le Sage, D. R. Slaughter, A. M. Tremaine, A. J. Wootton, P. T. Springer, and J. B. Rosenzweig. Experimental characterization of an ultrafast thomson scattering x-ray source with three-dimensional time and frequency-domain analysis. *Phys. Rev. ST Accel. Beams*, 7:060702, Jun 2004.

[14] C. Bula, K. T. McDonald, E. J. Prebys, C. Bamber, S. Boege, T. Kotseroglou, A. C. Melissinos, D. D. Meyerhofer, W. Ragg, D. L. Burke, R. C. Field, G. Horton-Smith, A. C. Odian, J. E. Spencer, D. Walz, S. C. Berridge, W. M. Bugg, K. Shmakov, and A. W. Weidemann. Observation of nonlinear effects in compton scattering. *Phys. Rev. Lett.*, 76:3116–3119, Apr 1996.

[15] P. Cardarelli, G. D. Domenico, M. Marziani, I. Muçollari, G. Pupillo, F. Sisini, A. Taibi, and M. Gambaccini. Energy distribution measurement of narrow-band ultrashort x-ray beams via k-edge filters subtraction. *Journal of Applied Physics*, 112(7):074908, 2012.

[16] Z. Chi, L. Yan, Z. Zhang, Z. Zhou, L. Zheng, D. Wang, Q. Tian, W. Wang, Z. Nie, J. Zhang, Y. Du, J. Hua, J. Shi, C. Pai, W. Lu, W. Huang, H. Chen, and C. Tang. Diffraction based method to reconstruct the spectrum of the thomson scattering x-ray source. *Review of Scientific Instruments*, 88(4):045110, 2017.

[17] K. Chouffani, F. Harmon, D. Wells, J. Jones, and G. Lancaster. Determination of electron beam parameters by means of laser-compton scattering. *Phys. Rev. ST Accel. Beams*, 9:050701, May 2006.

[18] A. H. Compton. A quantum theory of the scattering of x-rays by light elements. *Phys. Rev.*, 21:483–502, May 1923.

[19] T. J. Davis, D. Gao, T. E. Gureyev, A. W. Stevenson, and S. W. Wilkins. Phase-contrast imaging of weakly absorbing materials using hard x-rays. *Nature*, 373:595 EP –, 02 1995.

[20] J. de Haas, P. Dorenbos, and C. van Eijk. Measuring the absolute light yield of scintillators. *Nuclear Instruments and Methods in Physics Research Section A: Accelerators, Spectrometers, Detectors and Associated Equipment*, 537(12):97 – 100, 2005. Proceedings of the 7th International Conference on Inorganic Scintillators and their Use in Scientific adn Industrial Applications.

[21] Y. . Du, L. . Yan, J. . Hua, Q. . Du, Z. . Zhang, R. . Li, H. . Qian, W. . Huang, H. . Chen, and C. . Tang. Generation of first hard x-ray pulse at tsinghua thomson scattering x-ray source. *Review of Scientific Instruments*, 84(5):053301, 2013.

[22] A. Ferrari, P. R. Sala, A. Fasso, J. Ranft, O. Européenne, P. La, R. Nucléaire, A. Ferrari, P. R. Sala, A. Fassò, and J. Ranft. Fluka: a multi-particle transport code. In *CERN 2005-10 (2005), INFN/TC 05/11, SLAC-R-773*.

[23] G. Fiocco and E. Thompson. Thomson scattering of optical radiation from an electron beam. *Phys. Rev. Lett.*, 10:89–91, Feb 1963.

[24] M. Fujiwara, K. Kawase, and A. T. Titov. Parity nonconservation measurements with photons at spring8. *AIP Conference Proceedings*, 802(1):246–249, 2005.

[25] R. Gardner and K. Verghese. On the solid angle subtended by a circular disc. *Nuclear Instruments and Methods*, 93(1):163 – 167, 1971.

[26] D. J. Gibson, F. Albert, S. G. Anderson, S. M. Betts, M. J. Messerly, H. H. Phan, V. A. Semenov, M. Y. Shverdin, A. M. Tremaine, F. V. Hartemann, C. W. Siders, D. P. McNabb, and C. P. J. Barty. Design and operation of a tunable mev-level compton-scattering-based γ-ray source. *Phys. Rev. ST Accel. Beams*, 13:070703, Jul 2010.

[27] G. Golovin, S. Banerjee, C. Liu, S. Chen, J. Zhang, B. Zhao, P. Zhang, M. Veale, M. Wilson, P. Seller, and D. Umstadter. Intrinsic beam emittance of laser-accelerated electrons measured by x-ray spectroscopic imaging. *Sci. Rep.*, 6:24622, 04 2016.

[28] D. Gustavson, J. Murray, T. Phillips, R. Schwitters, C. Sinclair, J. Johnson, R. Prepost, and D. Wiser. A backscattered laser polarimeter e+e storage rings. *Nuclear Instruments and Methods*, 165(2):177 – 186, 1979.

[29] R. Gwin and R. B. Murray. Scintillation process in csi(tl). i. comparison with activator saturation model. *Phys. Rev.*, 131:501–508, Jul 1963.

[30] J. F. Hainfeld, H. M. Smilowitz, M. J. O'Connor, F. A. Dilmanian, and D. N. Slatkin. Gold nanoparticle imaging and radiotherapy of brain tumors in mice. *Nanomedicine (London, England)*, 8(10):1601–1609, 10 2013.

[31] F. V. Hartemann, W. J. Brown, D. J. Gibson, S. G. Anderson, A. M. Tremaine, P. T. Springer, A. J. Wootton, E. P. Hartouni, and C. P. J. Barty. High-energy scaling of compton scattering light sources. *Phys. Rev. ST Accel. Beams*, 8:100702, Oct 2005.

[32] F. V. Hartemann, A. M. Tremaine, S. G. Anderson, C. P. J. Barty, S. M. Betts, R. Booth, W. J. Brown, J. K. Crane, R. R. Cross, D. J. Gibson, D. N. Fittinghoff, J. Kuba, G. P. Le Sage, D. R. Slaughter, A. J. Wootton, E. P. Hartouni, P. T. Springer, J. B. Rosenzweig, and A. K. Kerman. Characterization of a bright, tunable, ultrafast compton scattering x-ray source. *Laser and Particle Beams*, 22(3):221–244, 2004.

[33] Y. Hwang, G. Anderson, C. Barty, D. Gibson, R. Marsh, and T. Tajima. LLNL Laser-Compton X-ray Characterization. In *Proc. of International Particle Accelerator Conference (IPAC'16), Busan, Korea, May 8-13, 2016*, number 7 in International Particle Accelerator Conference, pages 1885–1888, Geneva, Switzerland, June 2016. JACoW. doi:10.18429/JACoW-IPAC2016-TUPOW052.

[34] Y. Hwang, G. Anderson, C. Barty, D. Gibson, R. Marsh, and T. Tajima. LLNL Laser-Compton X-Ray Characterization. In *Proc. of North American Particle Accelerator Conference (NAPAC'16), Chicago, IL, USA, October 9-14, 2016*, number 3 in North American Particle Accelerator Conference, pages 977–979, Geneva, Switzerland, Jan. 2017. JACoW. https://doi.org/10.18429/JACoW-NAPAC2016-WEPOB35.

[35] A. Jochmann, A. Irman, M. Bussmann, J. P. Couperus, T. E. Cowan, A. D. Debus, M. Kuntzsch, K. W. D. Ledingham, U. Lehnert, R. Sauerbrey, H. P. Schlenvoigt, D. Seipt, T. Stöhlker, D. B. Thorn, S. Trotsenko, A. Wagner, and U. Schramm. High resolution energy-angle correlation measurement of hard x rays from laser-thomson backscattering. *Phys. Rev. Lett.*, 111:114803, Sep 2013.

[36] A. Jochmann, A. Irman, U. Lehnert, J. Couperus, M. Kuntzsch, S. Trotsenko, A. Wagner, A. Debus, H.-P. Schlenvoigt, U. Helbig, S. Bock, K. Ledingham, T. Cowan, R. Sauerbrey, and U. Schramm. Operation of a picosecond narrow-bandwidth laser–thomson-backscattering x-ray source. *Nuclear Instruments and Methods in Physics Research Section B: Beam Interactions with Materials and Atoms*, 309(Supplement C):214 – 217, 2013.

[37] R. Klein, T. Mayer, P. Kuske, R. Thornagel, and G. Ulm. Beam diagnostics at the bessy i electron storage ring with compton backscattered laser photons: measurement of the electron energy and related quantities. *Nuclear Instruments and Methods in Physics Research Section A: Accelerators, Spectrometers, Detectors and Associated Equipment*, 384(2):293 – 298, 1997.

[38] R. Kuroda, H. Toyokawa, M. Yasumoto, H. Ikeura-Sekiguchi, M. Koike, K. Yamada, T. Yanagida, T. Nakajyo, F. Sakai, and K. Mori. Quasi-monochromatic hard x-ray source via laser compton scattering and its application. *Nuclear Instruments and Methods in Physics Research Section A: Accelerators, Spectrometers, Detectors and Associated Equipment*, 637(1, Supplement):S183 – S186, 2011. The International Workshop on Ultra-short Electron & Photon Beams: Techniques and Applications.

[39] W. P. Leemans, R. W. Schoenlein, P. Volfbeyn, A. H. Chin, T. E. Glover, P. Balling, M. Zolotorev, K. J. Kim, S. Chattopadhyay, and C. V. Shank. X-ray based subpicosecond electron bunch characterization using 90° thomson scattering. *Phys. Rev. Lett.*, 77:4182–4185, Nov 1996.

[40] R. J. Loewen. *A compact light source: Design and technical feasibility study of a laser-electron storage ring X-ray source*. PhD thesis, Stanford University, 2003.

[41] R. Marsh, G. Anderson, C. Barty, D. Gibson, and Y. Hwang. LLNL X-band RF Gun Results. In *Proc. of International Particle Accelerator Conference (IPAC'16), Busan, Korea, May 8-13, 2016*, number 7 in International Particle Accelerator Conference, pages 3993–3995, Geneva, Switzerland, June 2016. JACoW. doi:10.18429/JACoW-IPAC2016-THPOW026.

[42] R. Marsh, G. Anderson, C. Barty, D. Gibson, and Y. Hwang. LLNL X-band RF Gun Results. In *Proc. of International Particle Accelerator Conference (IPAC'16), Busan, Korea, May 8-13, 2016*, number 7 in International Particle Accelerator Conference, pages 3993–3995, Geneva, Switzerland, June 2016. JACoW. doi:10.18429/JACoW-IPAC2016-THPOW026.

[43] R. A. Marsh, F. Albert, S. G. Anderson, G. Beer, T. S. Chu, R. R. Cross, G. A. Deis, C. A. Ebbers, D. J. Gibson, T. L. Houck, F. V. Hartemann, C. P. J. Barty, A. Candel, E. N. Jongewaard, Z. Li, C. Limborg-Deprey, A. E. Vlieks, F. Wang, J. W. Wang, F. Zhou, C. Adolphsen, and T. O. Raubenheimer. Modeling and design of an x-band rf photoinjector. *Phys. Rev. ST Accel. Beams*, 15:102001, Oct 2012.

[44] R. A. Marsh, G. G. Anderson, S. G. Anderson, D. J. Gibson, C. P. J. Barty, and Y. Hwang. Performance of a second generation x-band rf photoinjector. Submitted to Phys. Rev. Accel. Beams, 2018.

[45] H. N. McQuaid, M. F. Muir, L. E. Taggart, S. J. McMahon, J. A. Coulter, W. B. Hyland, S. Jain, K. T. Butterworth, G. Schettino, K. M. Prise, D. G. Hirst, S. W. Botchway, and F. J. Currell. Imaging and radiation effects of gold nanoparticles in tumour cells. *Scientific Reports*, 6:19442 EP –, 01 2016.

[46] W. Mengesha, T. Taulbee, B. Rooney, and J. Valentine. Light yield nonproportionality of csi(tl), csi(na), and yap. *Nuclear Science, IEEE Transactions on*, 45(3):456–461, Jun 1998.

[47] G. A. Mourou, T. Tajima, and S. V. Bulanov. Optics in the relativistic regime. *Rev. Mod. Phys.*, 78:309–371, Apr 2006.

[48] M. Nikl. Scintillation detectors for x-rays. *Measurement Science and Technology*, 17(4):R37, 2006.

[49] H. Ohgaki, S. Sugiyama, T. Yamazaki, T. Mikado, M. Chiwaki, K. Yamada, R. Suzuki, T. Noguchi, and T. Tomimasu. Measurement of laser-induced compton backscattered photons with anti-compton spectrometer. *IEEE Transactions on Nuclear Science*, 38(2):386–392, Apr 1991.

[50] G. M. Onyshchenko, L. L. Nagornaya, V. G. Bondar, Y. Borodenko, O. V. Zelenskaya, E. N. Pirogov, and V. D. Ryzhikov. Comparative light yield measurements of oxide and alkali halide scintillators. *Nuclear Instruments and Methods in Physics Research Section A: Accelerators, Spectrometers, Detectors and Associated Equipment*, 537(12):394 – 396, 2005. Proceedings of the 7th International Conference on Inorganic Scintillators and their Use in Scientific adn Industrial Applications.

[51] F. H. O'Shea, O. Williams, G. Andonian, S. Barber, Y. Sakai, J. B. Rosenzweig, I. Pogorelsky, M. Fedurin, K. Kusche, and V. Yakimenko. Single shot diffraction of picosecond 8.7-kev x-ray pulses. *Phys. Rev. ST Accel. Beams*, 15:020702, Feb 2012.

[52] I. V. Pogorelsky, I. Ben-Zvi, T. Hirose, S. Kashiwagi, V. Yakimenko, K. Kusche, P. Siddons, J. Skaritka, T. Kumita, A. Tsunemi, T. Omori, J. Urakawa, M. Washio, K. Yokoya, T. Okugi, Y. Liu, P. He, and D. Cline. Demonstration of 8×10^{18}photons/second peaked at 1.8 å in a relativistic thomson scattering experiment. *Phys. Rev. ST Accel. Beams*, 3:090702, Sep 2000.

[53] N. D. Powers, I. Ghebregziabher, G. Golovin, C. Liu, S. Chen, S. Banerjee, J. Zhang, and D. P. Umstadter. Quasi-monoenergetic and tunable x-rays from a laser-driven compton light source. *Nat. Photon.*, 8(1):28–31, 01 2014.

[54] S. Rosa, C. Connolly, G. Schettino, K. T. Butterworth, and K. M. Prise. Biological mechanisms of gold nanoparticle radiosensitization. *Cancer Nanotechnology*, 8(1):2, 2017.

[55] P. A. Ross. A new method of spectroscopy for faint x-radiations. *J. Opt. Soc. Am.*, 16(6):433–437, Jun 1928.

[56] S. G. Rykovanov, C. G. R. Geddes, J.-L. Vay, C. B. Schroeder, E. Esarey, and W. P. Leemans. Quasi-monoenergetic femtosecond photon sources from thomson scattering using laser plasma accelerators and plasma channels. *Journal of Physics B: Atomic, Molecular and Optical Physics*, 47(23):234013, 2014.

[57] Y. Sakai, I. Gadjev, P. Hoang, N. Majernik, A. Nause, A. Fukasawa, O. Williams, M. Fedurin, B. Malone, C. Swinson, K. Kusche, M. Polyanskiy, M. Babzien, M. Montemagno, Z. Zhong, P. Siddons, I. Pogorelsky, V. Yakimenko, T. Kumita, Y. Kamiya, and J. B. Rosenzweig. Single shot, double differential spectral measurements of inverse compton scattering in the nonlinear regime. *Phys. Rev. Accel. Beams*, 20:060701, Jun 2017.

[58] Y. Sakai, I. Pogorelsky, O. Williams, F. O'Shea, S. Barber, I. Gadjev, J. Duris, P. Musumeci, M. Fedurin, A. Korostyshevsky, B. Malone, C. Swinson, G. Stenby, K. Kusche, M. Babzien, M. Montemagno, P. Jacob, Z. Zhong, M. Polyanskiy, V. Yakimenko, and J. Rosenzweig. Observation of redshifting and harmonic radiation in inverse compton scattering. *Phys. Rev. ST Accel. Beams*, 18:060702, Jun 2015.

[59] T. Shintake. Proposal of a nanometer beam size monitor for e+e linear colliders. *Nuclear Instruments and Methods in Physics Research Section A: Accelerators, Spectrometers, Detectors and Associated Equipment*, 311(3):453 – 464, 1992.

[60] P. Sprangle, A. Ting, E. Esarey, and A. Fisher. Tunable, short pulse hard xrays from a compact laser synchrotron source. *Journal of Applied Physics*, 72(11):5032–5038, 1992.

[61] C. Sun, J. Li, G. Rusev, A. P. Tonchev, and Y. K. Wu. Energy and energy spread measurements of an electron beam by compton scattering method. *Phys. Rev. ST Accel. Beams*, 12:062801, Jun 2009.

[62] P. Suortti and W. Thomlinson. Medical applications of synchrotron radiation. *Physics in Medicine & Biology*, 48(13):R1, 2003.

[63] E. Sysoeva, V. Tarasov, and O. Zelenskaya. Comparison of the methods for determination of scintillation light yield. *Nuclear Instruments and Methods in Physics Research Section A: Accelerators, Spectrometers, Detectors and Associated Equipment*, 486(12):67 – 73, 2002. Proceedings of the 6th International Conference on Inorganic Scin tillators and their Use in Scientific and Industrial Applications.

[64] T. Tajima and R. Li. Marriage of a 20kev superconducting xfel with a 100pw laser. 04 2018.

[65] D. P. Umstadter. All-laser-driven thomson x-ray sources. *Contemporary Physics*, 56(4):417–431, 2015.

[66] C. W. E. van Eijk. Inorganic scintillators in medical imaging. *Physics in Medicine and Biology*, 47(8):R85, 2002.

[67] T. Weitkamp, A. Diaz, C. David, F. Pfeiffer, M. Stampanoni, P. Cloetens, and E. Ziegler. X-ray phase imaging with a grating interferometer. *Opt. Express*, 13(16):6296–6304, Aug 2005.

[68] S. W. Wilkins, T. E. Gureyev, D. Gao, A. Pogany, and A. W. Stevenson. Phase-contrast imaging using polychromatic hard x-rays. *Nature*, 384:335 EP –, 11 1996.

[69] O. Williams, G. Andonian, M. Babzien, E. Hemsing, K. Kusche, J. Park, I. Pogorelsky, G. Priebe, J. Rosenzweig, and V. Yakimenko. Characterization results of the bnl atf compton x-ray source using k-edge absorbing foils. *Nuclear Instruments and Methods in Physics Research Section A: Accelerators, Spectrometers, Detectors and Associated Equipment*, 608(1):S18 – S22, 2009. Compton sources for X/ rays: Physics and applications.

[70] Y. K. Wu. Accelerator physics research and light source development at duke university. In *Proc. of International Particle Accelerator Conference (IPAC'10), Kyoto, Japan, May 23-28, 2010*, number 1 in International Particle Accelerator Conference, pages 2648–2650, Geneva, Switzerland, June 2010. JACoW.